Front. Optoelectron. China 2011, 4(1): 24–44
DOI 10.1007/s12200-011-0207-0

REVIEW ARTICLE

# Dye-sensitized solar cells based on ZnO nanotetrapods

**Wei CHEN[1,2], Shihe YANG (✉)[1]**

1 Department of Chemistry, The Hong Kong University of Science and Technology, Hong Kong, China
2 Wuhan National Laboratory for Optoelectronics, Huazhong University of Science and Technology, Wuhan 430074, China



**Abstract** In this paper, we reviewed recent systematic studies of using ZnO nanotetrapods for photoanodes of dye-sensitized solar cells (DSSCs) in our group. First, the efficiency of power conversion was obtained by more than 3.27% by changes of conditions of dye loading and film thickness of ZnO nanotetrapod. Short-circuit photocurrent densities ($J_{sc}$) increased with the film thickness, $J_{sc}$ would not be saturation even the film thickness was greater than 35 μm. The photoanode architecture had been charactered by good crystallinity, network forming ability, and limited electron-hopping interjunctions. Next, DSSCs with high efficiency was devised by infiltrating $SnO_2$ nanoparticles into the ZnO nanotetrapods photoanodes. Due to material advantages of both constituents described as above, the composite photoanodes exhibited extremely large roughness factors (*RF*s), good charge collection, and tunable light scattering properties. By varying the composition of the composite photoanodes, we had achieved an efficiency of 6.31% by striking a balance between high efficiency of charge collection for $SnO_2$ nanoparticles rich films and high light scattering ability for ZnO nanotetrapods rich films. An ultrathin layer of ZnO was found to form spontaneously on the $SnO_2$ nanoparticles, which primarily was responsible for enhancing open-circuit photovoltage ($V_{oc}$). We also identified that recombination in $SnO_2$/ZnO composite films was mainly determined by ZnO shell condition on $SnO_2$, whereas electron transport was greatly influenced by the morphologies and sizes of ZnO crystalline additives. Finally, we applied the composite photoanodes of $SnO_2$ nanoparticles/ZnO nanotetrapods to flexible DSSCs by low temperature technique of "acetic acid gelation-mechanical press-ammonia activation." The efficiency has been achieved by 4.91% on ITO-coated polyethylenenaphtalate substrate. The formation of a thin ZnO shell on $SnO_2$ nanoparticles, after ammonia activation, was also found to be critical to boosting $V_{oc}$ and to improving inter–particles contacts. Mechanical press, apart from enhancing film durability, also significantly improved charge collection. ZnO nanotetrapods had been demonstrated to be a better additive than ZnO particles for the improvement of charge collection in $SnO_2$/ZnO composite photoanodes regardless of whether they were calcined.

**Keywords** dye-sensitized solar cell (DSSC), metal oxides, nanostructure, ZnO nanotetrapod, photoanode, flexible solar cell

## 1 Introduction

Photoelectrodes of dye sensitized solar cells (DSSCs) are nanostructured by nature for effectively ferrying electrons and holes [1,2]. The rapid advances of nanomaterials and nanotechnology in recent years are therefore propitious in promoting the development of DSSCs [3]. The nanoscale engineering of new photoelectrode architectures should not only enhance our understanding of the inherent working of DSSCs but also help to improve the cell performance, especially in the emerging frontiers such as flexible DSSCs and solid-state DSSCs [4–8]. In a series of recent work, we have demonstrated the viability of new photoanode architectures in DSSCs comprising building blocks of ZnO nanoplates [9], ZnO nanotetrapods [7,10,11] and $TiO_2$ nanospindles [12]. This article we reviewed our systemic studies on DSSCs based on ZnO nanotetrapods related photoanodes, namely, pure ZnO nanotetrapods based photoanode [7], ZnO nanotetrapods/$SnO_2$ nanoparticles composite photoanode with [10] and without calcination [11].

Although $TiO_2$ nanoparticles are still the most efficient photoanode material of DSSC, there are many for improvement in terms of charge transport and recombination suppression by designing new nanostructured photoanodes [2,13,14]. In addition, novel different nanostructures are also important in meeting the challenges of developing flexible DSSCs and solid state DSSCs. Various

Received October 18, 2010; accepted December 30, 2010

E-mail: chsyang@ust.hk

new nanostructures have been tested for applications in DSSC, especially one-dimensional (1D) nanoarrays, which when used as photoanodes exhibit superiority in electron transport [5,13–15]. However, their DSSC performances have been limited by practical problems such as lack of control over nanostructures during materials fabrication processes.

For $TiO_2$ based DSSCs on flexible polymer substrates, the best efficiency reported is 7.4% [16], which is still much lower than those based on the traditional high temperature calcined $TiO_2$ photoanodes [17]. A common problem of the low temperature treated $TiO_2$ photoanodes consists in the poor electrical contacts between the $TiO_2$ nanoparticles, which hinder charge collection in the photoanode [18]. In the past few years, many strategies [16,18–21] have been attempted to address this issue but no significant improvement. This status quo raises the question about whether $TiO_2$ nanoparticles are the best choice for the photoanodes of flexible DSSCs. In fact, ZnO is known to be much more versatile nanostructural former since numerous well-defined nanostructures of ZnO have been generated even under mild conditions [22]. Understandably, ZnO, being chemically more reactive, is more amenable to crystallization and morphological transformations under mild conditions. As has also been demonstrated, low-temperature treated ZnO photoanodes achieved even better DSSC performance than those obtained at high temperature [23,24]. Therefore, replacing $TiO_2$ with ZnO seems to be a reasonable direction toward flexible DSSCs [8,25].

Research results in controlled synthesis of ZnO nanotetrapods achieved by our group [26] prompted us to apply such a novel nanostructure to DSSC [7]. Hsu et al. reported ZnO tetrapods based DSSCs with 1.2% efficiency. The relatively low efficiency is due to the use of large size tetrapods (about 5 μm in arm length and hundreds of nm in arm diameter) and a gelation additive of zinc acetic ($ZnAc_2$) for assisting film formation [26]. Besides, the thermal decomposition of $ZnAc_2$ could introduce undesired impurities. In contrast, we used well-crystallized ZnO nanotetrapods (about 500 nm in arm length and 40 nm in arm diameter) to construct photoanodes [27]. We found that the formation of pure nanotetrapod photoanode film did not need any binder in the film-preparation paste and the calcination step, because the numerous contacts among the tangled nanotetrapods gave the film sufficient mechanical stability. As a result, a decent power conversion efficiency of 3.27% was achieved even when the film was not calcined. This was the first time that DSSC based on pure ZnO nanotetrapod photoanode was demonstrated with a reasonable efficiency; simply by physically contacting the nanotetrapods, the branched nanotetrapods network could effectively transport photoinduced electrons. Later on, Chiu et al. [28] and Bacsa et al. [29] also reported studies on ZnO nanotetrapods based DSSCs with their photoanodes all calcined at high temperatures.

Literally, the ZnO nanotetrapods photoanode for DSSC is noteworthy in the following aspects: 1) ZnO nanotetrapods as a branched 1D nanomaterial with excellent crystallinity can significantly reduce the numerous electron-hopping interjunctions existing in the porous nanoparticle films, and therefore promote charge transport and suppress carrier recombination; 2) The radiating branches of the ZnO nanotetrapods equip them with the ability to form mechanically robust network films; 3) The well-defined nanotetrapods network permits easy blending with other additives such as $SnO_2$ nanoparticles; 4) The outstanding network forming ability of the well-crystallized ZnO nanotetrapods should also permit low-temperature processing of photoanodes needed for flexible DSSCs; 5) Unlike ZnO nanowire arrays which need be grown in situ and hence are unsuitable for large-scale production, the ZnO nanotetrapods photoanode films should be easily fabricated on flexible substrates in a roll-to-roll fashion. These advantageous features make the ZnO nanotetrapods a preferred photoanode material for DSSCs, particularly flexible DSSCs [25]. Indeed, on the basis of our work in the past few years, the ZnO nanotetrapods have fulfilled our expectation as a novel photoanode material for DSSCs, and added new perspectives on the important roles nanostructures can play in DSSCs.

This review is organized as follows. First, we will summarize our work on pure ZnO nanotetrapods based DSSCs. Second, the work on the composite photoanode of $SnO_2$ nanoparticles/ZnO nanotetrapods will be discussed. Third, our application study of the nanomaterial system in flexible DSSCs will be reconsidered. Finally, we will present conclusions and prospects about the use of ZnO nanotetrapods in DSSCs.

## 2 ZnO nanotetropod photoanode

The crack-free, extremely open porous structure of a 30 μm thick ZnO nanotetrapod film can be appreciated from Figs. 1(a)–1(c), which was prepared by the doctor blade method. Of note, besides butanol solvent, no binder or corrosive additive was contained in the film-preparation paste in preparing the ZnO nanotetrapods film, which made it possible for us to sidestep the calcination procedure by just evaporation away the volatile solvent at about 80°C. A close-up view of the ZnO nanotetrapods' film in Fig. 1(d) catches some details of the inter-tetrapod connections. It can be observed clearly that the nanotetrapods are well connected with at least one stout contact for each neighboring pair. Such inter-tetrapod connections are held responsible for the structural stability of the hollow film and also secure continuous electron transport pathways, as schematically illustrated in Fig. 1(e). Although with such zigzag electron transport pathways instead of the straight-through pathways of well-aligned

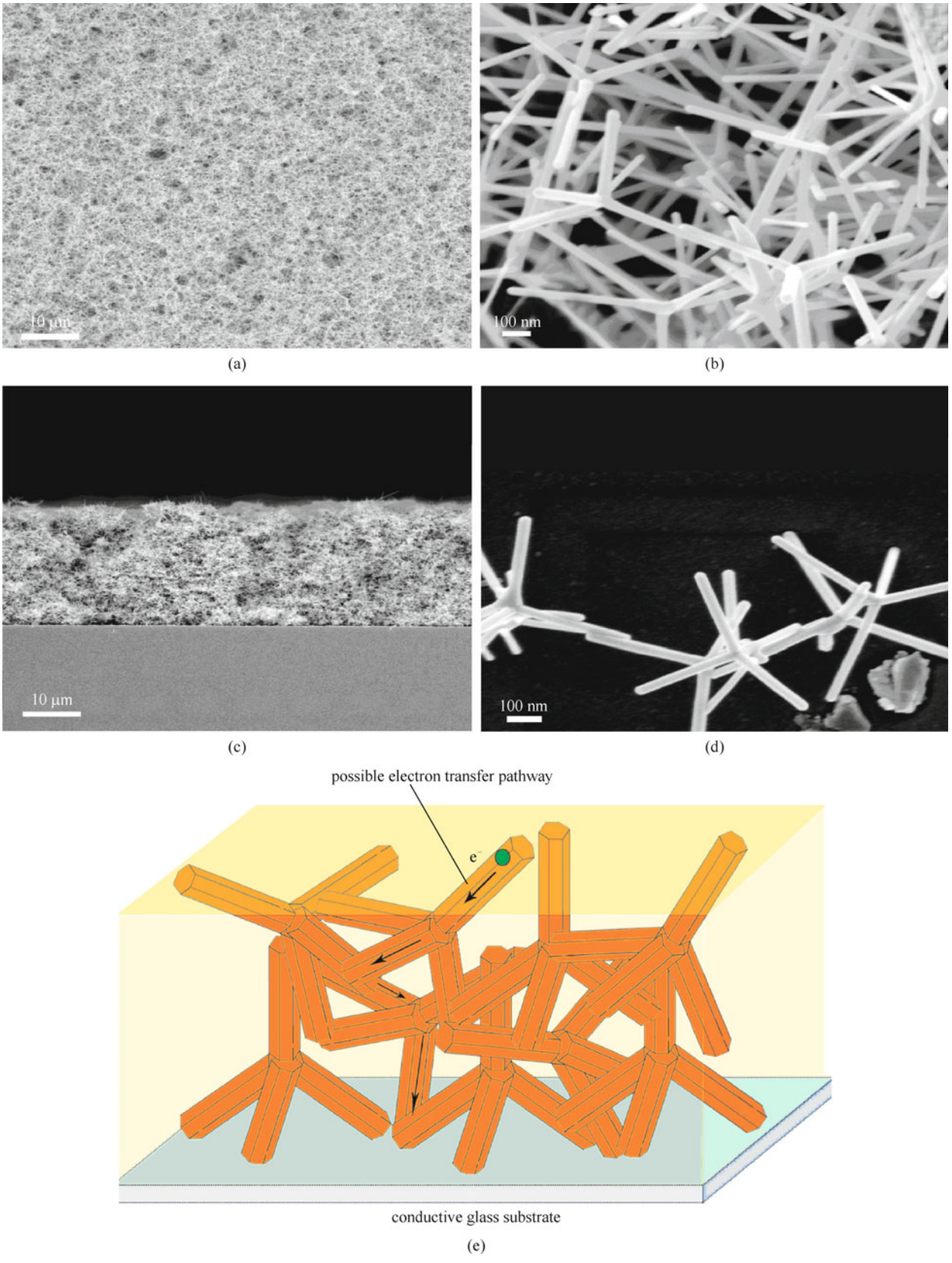


**Fig. 1** Structural characteristics of 30 μm thick ZnO nanotetrapod film. SEM images viewed from top (a), at high resolution (b), in cross-section (c), and at detailed inter-tetrapod connections (d); (e) schematic showing a possible electron transport pathway across the ZnO nanotetrapod film. Sample in (d) was from residue left on FTO-glass substrate after scratching away nanotetrapods film. (Ref. [7], published with permission)

nanowire arrays, the nanotetrapod's film should still exhibit better charge transport than nanoparticle films, simply because the branched structure of the nanotetrapods ensures that at least one of its four arms roughly points to the direction perpendicular to the conductive glass substrate. As a consequence, the average number of interjunctions across which photoinjected electrons in the nanotetrapods film need to pass along the perpendicular direction in order to be collected at the anode should be over two orders of magnitude lower than that of common nanoparticle photoanodes. This can be appreciated simply from the size ratio of nanotetrapods (500–800 nm in arm length) to nanoparticles (10–20 nm in diameter).

As a most popularly used dye for the research of $TiO_2$ DSSCs, N719 was also employed in the present study although it is by no means an optimized dye for the ZnO nanotetrapods based DSSCs. The dye loading conditions including the dye concentration in ethanol and the corresponding dye loading time have been optimized for the ZnO nanotetrapods films with different thicknesses by monitoring the adsorbed amount of dye as well as the resulting short-circuit photocurrent densities ($J_{sc}$) of the corresponding DSSCs. $J_{sc}$ was found to first increase on dye loading time and then gradually decrease; the optimized dye loading time $t_{opt}$ for the $J_{sc}$ peak was not sensitive to film thickness but depended greatly on dye concentration. Increasing dye concentration from 0.3 mM to 0.1 mM raised $t_{opt}$ from 20 to 75 min, and also improved the saturated $J_{sc}$. Such optimization of dye loading condition is especially important for acidic dye sensitized ZnO photoanodes because one needs to balance the maximum dye adsorbing density on ZnO surface and the minimum corrosion of the ZnO nanostructure; the latter often yields Zn-dye complexes which could hinder electron injection [30,31].

Under the optimized dye loading condition, the optimum performance of the ZnO nanotetrapods based DSSCs was $J_{sc} = 9.71\ mA \cdot cm^{-2}$, open-circuit photovoltage ($V_{oc}$) = 614 mV, fill factors ($FF$) = 0.55, and efficiency = 3.27% at the photoanode thickness of 31.1 μm, as shown in Fig. 2(a). Such performance is a little bit lower than that of the recently reported ZnO nanoparticle photoanode fabricated at room temperature on flexible substrate (efficiency = 3.8%) [23]. However, it represents a significant improvement over the best DSSC based on a well-aligned ZnO nanorod array photoanode: about 60% higher in $J_{sc}$ mainly due to a higher $RF$ of our nanotetrapods film (350 for the about 30 μm thick nanotetrapods film versus 200 for the 20 μm thick nanorod arrays film), about 50% higher in $FF$, and as a consequence nearly 120% higher in overall efficiency [13]. A higher efficiency was reported subsequently by Chiu et al. on a similar system primarily thanks to their use of an organic D149 dye with higher extinction coefficient, in addition to the necessary calcination procedure [28].

Figure 2(b) plots the amount of dye loading versus the nanotetrapod film thickness and $RF$, which are related by a proportionality factor. The $RF$ of our nanotetrapod film is calculated to be 11.2 $\mu m^{-1}$, by multiplying the BET surface area (18.56 $m^2 \cdot g^{-1}$) with the weight of a ZnO nanotetrapod film with a given area and thickness, and then divided by the projected area of the film on the glass substrate. The dependence of cell performance on nanotetrapods' film thickness, and therefore $RF$ and the amount of dye loading as revealed in Fig. 2(b), is shown in Figs. 2(c) and 2(d). First, $J_{sc}$ increases sub-linearly to 10.31 $mA \cdot cm^{-2}$ with film thickness up to about 36.0 μm ($RF$ = 403.2), while the efficiency has reached the saturation level of 3.27% at a relatively small thickness of about 31.1 μm ($RF$ = 348.3). In most cases of nanoparticle photoanodes, the optimum film thickness, beyond which $J_{sc}$ begins to decrease, is in the range of 10–20 μm [13], mainly limited by the effective electron diffusion length ($L_n$). A film thicker than $L_n$ will not result in higher $J_{sc}$, but only increase dark current. Obviously, $L_n$ of our nanotetrapods film is at least $> 36.0$ μm, highlighting the efficient electron collection of our nanotetrapods photoanode even without calcination. It can be observed from Fig. 2(d) that, $V_{oc}$ decreases from 780 to 596 mV and $FF$ decreases from 0.61 to 0.49 as the film thickness increases from 5.3 to 36.0 μm, such data was maintained at relative high level among that of the reported dye sensitized ZnO solar cells [13,32]. Also included in Figs. 3(c) and 3(d) for comparison are data from some of other nanotetrapods films, which were calcined at 450°C in air for 30 min. It can be seen that there is nearly no performance difference between the solar cells based on calcined and non-calcined nanotetrapods photoanodes. Plausibly, the calcination temperature of 450°C, which is commonly used and effective on $TiO_2$ and ZnO nanoparticles photoanodes, may be too low to have noticeable effect on the bonding between the nanotetrapods.

Electrochemical impedance spectroscopy (EIS) is a powerful technique to study the kinetics of complex interface processes in DSSCs [33,34]. Under appropriate conditions, electron transport in the active film, electron recombination at the semiconductor-electrolyte interface, charge transfer at the counter electrode, and diffusion of redox species in the electrolyte can be disentangled as a function of frequency by virtue of equivalent circuit models. For our ZnO nanotetrapod's photoanodes, two distinct features need to be clarified: one is the non-necessity of the calcination procedure and the other is the excellent electron collection property. To our surprise, no obvious difference on the EIS spectral features could be detected for the ZnO nanotetrapods' films with and without calcination. As EIS is very sensitive to interface changes, the similar EIS results indicate that the interface structure did not undergo significant change upon calcinations, which is consistent with the little change in cell performance due to calcination described above.

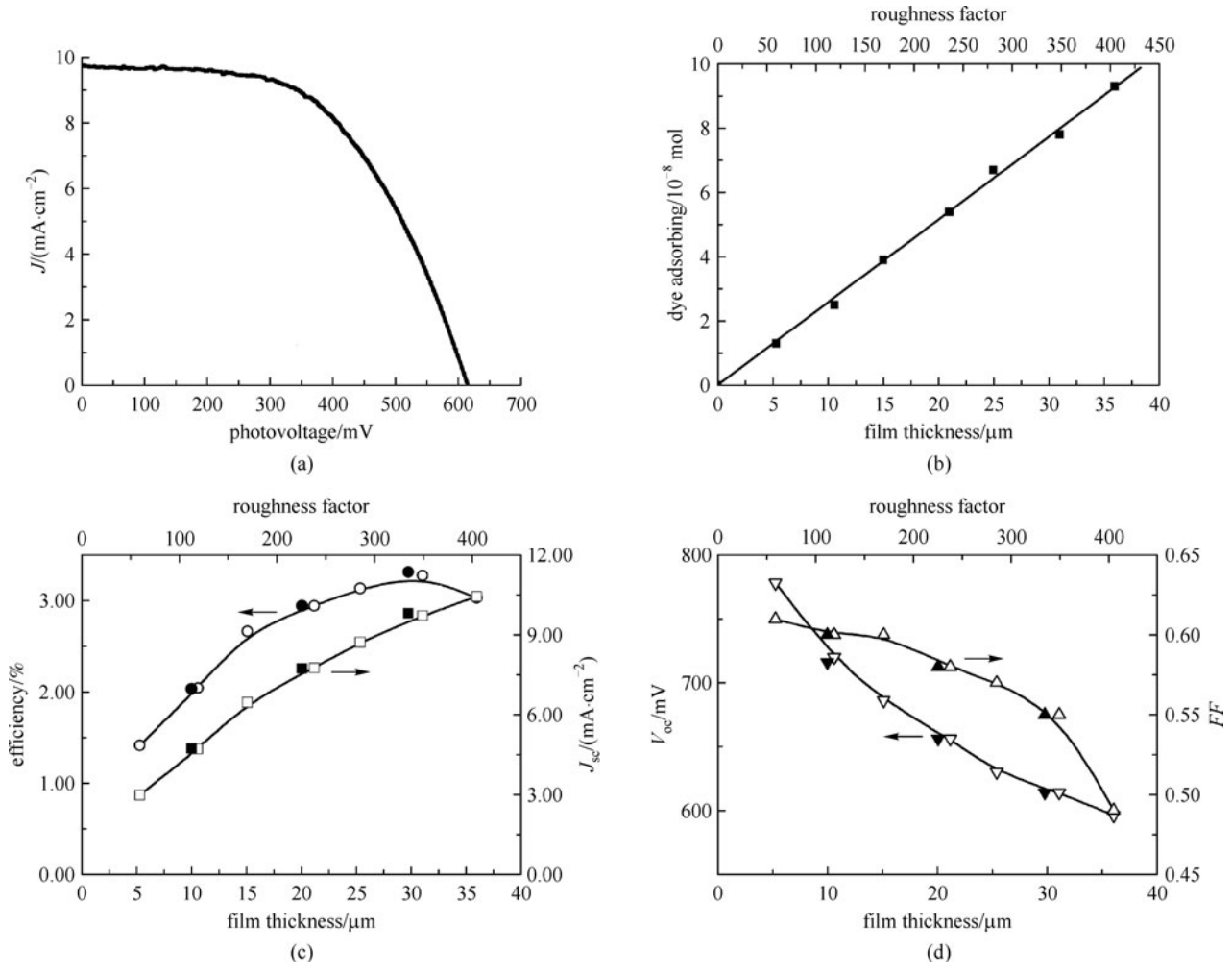


**Fig. 2** (a) *J-V* characteristic curve of typical ZnO nanotetrapod cell with film thickness of 31.1 μm; (b) dependence of dye loading amount on film thickness ($\propto RF$); dependence of cell performance on film thickness including overall solar conversion efficiency and short-circuit photocurrent density (c) and open-circuit photovoltage and fill factor (d). Open symbols and solid symbols in (c), (d) correspond to nonclacined and calcined photoanodes, respectively (Ref. [7], published with permission)

As an example, shown in Fig. 3 are the EIS Nyquist plots for two ZnO nanotetrapod photoanodes (with thickness of 10.2 and 21.3 μm, respectively), which were taken at an applied potential of $-0.3$ V, under 0.1 sun illumination. The spectra exhibit Warburg-like diffusion lines (short straight lines with a slope of approximately 1) in the high frequency region, corresponding to the electron transport process across the photoanode film, followed by big semicircles toward the low frequency region, representing the solid-electrolyte interfacial charge recombination process. According to the well documented diffusion-recombination model [35,36], we can use the following equation to fit impedance spectra in the low frequency region,

$$Z = \frac{1}{3}R_t + \frac{R_r}{1 + i\omega/\omega_r}, \quad (1)$$

where $R_t$ is electron transport resistance, $R_r$ is interfacial recombination resistance, $\omega_r$ is characteristic frequency of recombination, and $\omega$ is angular frequency of applied AC voltage. From the fitting procedure, $R_t$ and $R_r$ for the 10.2 μm photoanode are estimated to be 300 and 9000 Ω, respectively, and for the 21.3 μm photoanode are 640 and 17300 Ω, respectively. A simple estimate gives the charge collection efficiencies ($\eta_{mL} = 1 - R_t/R_r$ [37]) of about 100%, suggesting that at least for the photoanodes with thicknesses up to 21.3 μm and at the applied potential of $-0.3$ V, most of the photoinjected electrons can reach the conductive glass substrate by diffusion before recombination. This result demonstrates the long effective electron diffusion length of the ZnO nanotetrapods films and explains why $J_{sc}$ of our nanotetrapods DSSCs is still below the saturation point even when the film thickness has been increased up to $> 20$ μm. Such a long effective diffusion length has also been verified by Chiu et al. [28].

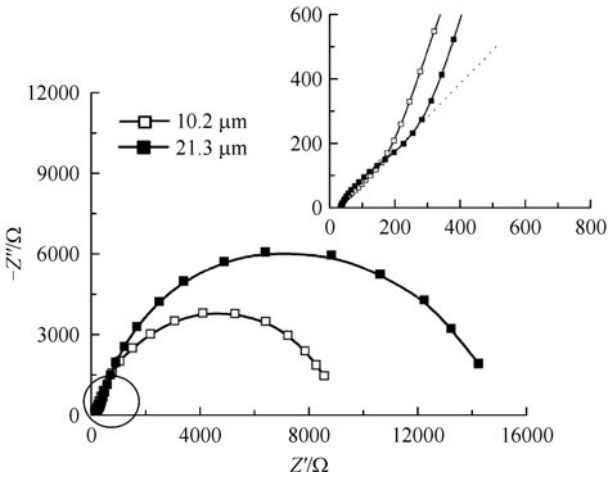


**Fig. 3** Impedance spectra of DSSCs based on ZnO nanotetrapods photoanodes with different film thicknesses, at applied potential of –0.3 V under 0.1 sun illumination. Inset shows enlarged portion of circled area, dotted line highlights Warburg-like diffusion lines (Ref. [7], published with permission)

## 3 $SnO_2$ nanoparticles/ZnO nanotetrapods composite photoanode

To increase surface areas of the ZnO nanotetrapods based photoanodes to promote light harvesting, a reasonable consideration is to introduce apposite nanoparticles into the nanotetrapod matrix given that there is ample space left between the nanotetrapods. Key to the idea is that the ZnO nanotetrapods' network figures as a global electron transport highway while the encapsulated nanoparticles serve to increase the *RF* and take part in the local charge transport [4,38,39]. Similar scheme has been practiced in nanoparticles/nanowires composite systems [4,6,38,40,41], but in most of these cases, the constituent nanoparticles and nanowires were of the same material [38]. We employed $SnO_2$ nanoparticles for this purpose largely based on the following considerations: 1) DSSCs based on $SnO_2$/ZnO nanoparticles composites have been demonstrated and the synergy between the components has been discussed [42,43]; 2) $SnO_2$, being more stable than $TiO_2$ and ZnO, is more amenable for film formation via sol-gel reactions at moderate temperatures; 3) Our survey experiments on blending in $TiO_2$ nanoparticles, albeit with increased $V_{oc}$, resulted in significantly reduced $J_{sc}$, which was also revealed in photoanodes consisting of $TiO_2$ nanoparticles/ZnO nanowire arrays blends [6,40]. On top of these, a proper electronic structure combination of the components, e.g., conduction band edge positions [44], distribution of accepting states in the conduction bands [39], is critical to the performance of the composite photoanodes. In practice, different surface chemistry of the constituents has to be duly considered.

### 3.1 Nanostructural characterizations

We synthesized the $SnO_2$ nanoparticles with an average size of about 5–10 nm using a modified hydrothermal recipe [45]. Good monodispersity and suitable size combination of the $SnO_2$ nanoparticles and the ZnO nanotetrapods allowed ready formation of 3D interpenetrating network films. In our experience, a higher content of ZnO nanotetrapods is more helpful to stabilizing the composite film by releasing any locally accumulated, capillary force induced stress during the film drying process when freshly deposited on a FTO glass substrate, leading to better-adhered composite films to the substrate with minimal micron sized cracks. On the other hand, when more ZnO nanotetrapods were blended, the film became hollower and more optically opaque due to the light scattering effect. This is revealed the diffuse reflectance spectra in Fig. 4. The reflectance spectra appear to abide by the Mie scattering theory, which states that pores with a comparable size to the light wavelength can act as effective light scattering centers [46,47]. Understandably, light scattering in the pure $SnO_2$ nanoparticles film is nearly negligible because the pores inside the film are too small ($< 20$ nm) to act as effective scattering centers. However, the diffuse reflectance of the composite films increases dramatically and monotonously with the increase of the ZnO content, culminating in the pure ZnO nanotetrapods films. Notably, a substantial fraction of visible light is scattered back. This is not surprising because when more ZnO nanotetrapods are blended with $SnO_2$ nanoparticles, more pores will be generated with sizes closer to ideal for light scattering, e.g., 50–100 nm, as suggested by Hore et al. [46]. This has been corroborated by our nitrogen adsorption-desorption measurements [10].

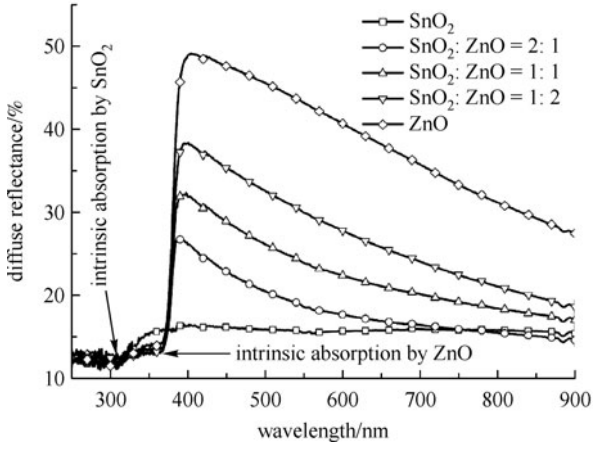


**Fig. 4** Diffuse reflectance spectra of pure $SnO_2$ nanoparticles film, pure ZnO nanotetrapods film and three $SnO_2$ nanoparticles/ZnO nanotetrapods composite films. All films are prepared with same thicknesses of around 6 μm on glass slides (Ref. [10], published with permission)

To study how the ZnO shell condition on the $SnO_2$ nanoparticles influences the cell performance, we carried out high resolution TEM-EDX and XPS measurements. Although no evident core-shell structure could be observed by high resolution TEM due to the thinness of the layer, the Zn signal could always be detected by EDX analysis in the region of pure $SnO_2$ nanoparticles. Using an atomic ratio of 2%–5% for Zn/Sn in the $SnO_2$ nanoparticles region, and assuming ideal spheres of 8 nm diameter for the $SnO_2$ nanoparticles, we estimate the ZnO shell to be only 1 to 2 atomic layers thick. More important, the XPS study supports the presence of Sn-O-Zn bonds between the $SnO_2$ core and the ZnO shell evidently, by the comparison of the Sn $3d_{5/2}$ spectra of the composite films and the pure $SnO_2$ film, as shown in Fig. 5. The Sn $3d_{5/2}$ peak is shifted to a lower energy for the composite films (486.20 eV) from that of the pure $SnO_2$ film (486.65 eV). The lower electrophilicity of $Zn^{2+}$ in the shell than that of $Sn^{4+}$ in the core should be responsible for the down-shift of the Sn $3d_{5/2}$ peak upon the formation of the ultrathin ZnO shell. Besides, the peak position at 486.20 eV is independent of the composition for the three composite films, indicating a similar ZnO shell coverage and thickness on $SnO_2$ under the same treatment conditions. In relation to the origin of the core-shell structure, we suspect that it stem from the chemical instability of ZnO in a polar solvent; the alkaline ZnO tends to be deposited on the relatively acidic surface of $SnO_2$ [48].

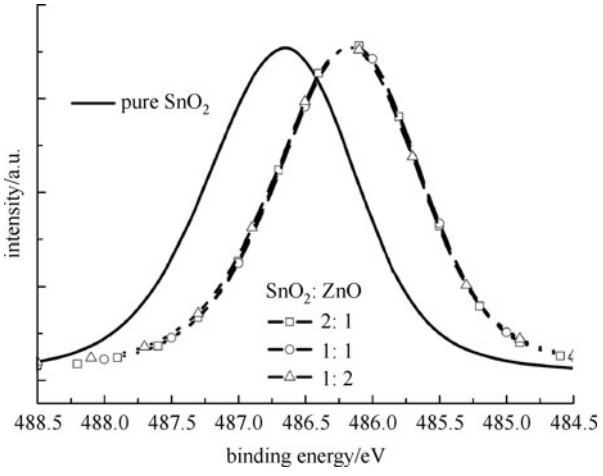


**Fig. 5** Sn $3d_{5/2}$ XPS spectra of pure $SnO_2$ nanoparticles film and the three composite films (Ref. [10], published with permission)

### 3.2 Performance appraisal of the DSSCs

Presented in Fig. 6 are the performance test results of the DSSCs based on the three series of composite films under 1 Sun AM 1.5G simulated solar light. The corresponding data for the pure $SnO_2$ nanoparticles film and for the pure ZnO nanotetrapods film [7] are also included for comparison. Significantly, the *RF* values for the three series of composite films can exceed 1600, much higher than that of the pure ZnO nanotetrapods film and also comparable to those of the most efficient $TiO_2$ nanoparticles photoanodes [49]. It is noticed that the dye adsorbing amount per *RF* for the pure $SnO_2$ film is obviously lower than those of composite films due probably to the more basic surfaces of the latter, i.e., the ZnO ultrathin layer modified $SnO_2$ surfaces [48].

The dependence of short-circuit photocurrent density, $J_{sc}$, on film thickness exhibits obviously nonlinear arc-shaped trends (Fig. 6(b)) for all except the ZnO nanotetrapods films. For the three series of composite films with $SnO_2$:ZnO = 2:1, 1:1 and 1:2 compositions, $J_{sc}$ become saturated at about 7, 10 and 15 μm, respectively. At the thicknesses of the saturated $J_{sc}$, the *RF* and dye adsorbing amount are nearly the same, which are about 1600 and in the range of $2.0 \times 10^{-7} - 2.4 \times 10^{-7}$ mol·cm$^{-2}$, respectively. The nonlinear trends of $J_{sc}$ versus *RF* (dye adsorbing amount) and their saturated positions should be due primarily to the Beer's Law, which is related to the light harvesting efficiency (*LHE*) of a photoanode through the equation $LHE(\lambda) = 1 - 10^{-\varepsilon\Gamma}$ [50], where $\Gamma$ is the surface coverage of dye (mol·cm$^{-2}$) and $\varepsilon$ is the dye's molar absorption coefficient (mol$^{-1}$ cm$^2$) at wavelength $\lambda$. Additionally, light scattering effect as revealed by diffuse reflectance spectra of the three composite films also needs be considered; the light scattering effect could cause deviation from the Beer's law [50] and thus may be partially responsible for different arc shapes of the $J_{sc}$–thickness plots.

$V_{oc}$ values (600–660 mV) of the three composite films (Fig. 6(c)) are found to lie between those of the pure $SnO_2$ nanoparticles film and the pure ZnO nanotetrapod's film but much closer to the latter. The origin of the $V_{oc}$ enhancement of $SnO_2$/ZnO composite photoanodes in comparison to pure $SnO_2$ has been debated since the first report on this subject [51]. Early on, researchers generally ascribed the $V_{oc}$ enhancement to the functioning of the thin ZnO shell to suppress recombination [48,51]. Our IMVS and XPS results [10] show that the band edge up-shift due to the ZnO shell formation on the $SnO_2$ surface plays the key role, which can be taken as the new evidences supporting Niinobe et al.'s viewpoint [43]. The $V_{oc}$ dependences for the three composite films on thickness are similar (see Fig. 6(d)): first increase and then decrease, a phenomenon which seems to be at odd with the previously reported monotonically decreasing trend of $V_{oc}$ with film thickness [38,45]. This could be attributed to the uncontrolled dark current loss through the bare FTO substrate (there was no blocking layer in our composite photoanode) which would give rise to nonmonotonical variation of $J_{inj}/J_{dark}$ and therefore $V_{oc}$ according to the equation of $V_{oc} = (k_B T/q)\ln(J_{inj}/J_{dark})$ [2], where $k_B$, $q$ and $T$ is Boltzmann constant, electron charge and absolute

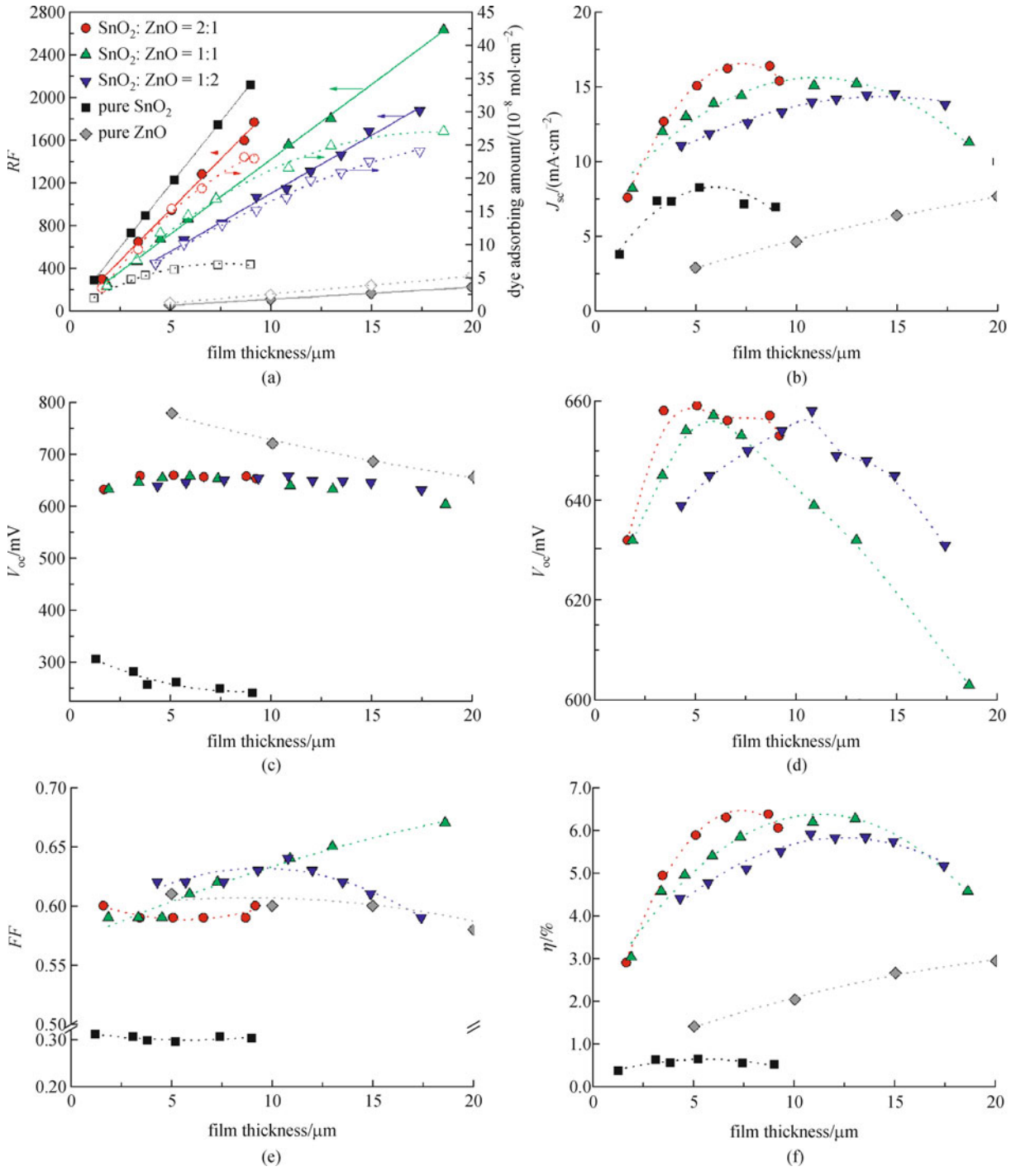


**Fig. 6** Thickness dependent characteristics of $SnO_2$ nanoparticles/ZnO nanotetrapods composite films as well as pure $SnO_2$ nanoparticles film and pure ZnO nanotetrapods film. (a) *RF* (denoted by solid symbols) and dye adsorbing amount (denoted by open symbols); (b) short-circuit photocurrent density $J_{sc}$; (c) open-circuit photovoltage $V_{oc}$; (d) a blown-up region highlights $V_{oc}$ of three composite films; (e) fill factor *FF* and (f) overall energy conversion efficiency $\eta$ (Ref. [10], published with permission)

temperature, respectively, and $J_{inj}$ is injected photocurrent density from dye to the semiconductor and $J_{dark}$ is dark current due to the recombination at semiconductor/electrolyte interface. *FF* for the three composite films vary within the range of 0.55 to 0.70 (Fig. 6(e)) depending on the thickness, which are generally higher than that of pure $SnO_2$ nanoparticles films and comparable to that of pure ZnO nanotetrapods films. Although the unexpected *FF* dependences on film thickness remain to be explained, complications arising from the peculiar nanostructures and

their combinations, uncontrolled dye corrosion on ZnO in the composite films, etc. may play a part.

Maximum cell efficiencies for the three composite films obtained from Fig. 6(f) are listed in Table 1. The efficiencies up to 6.31% are a dramatic improvement over the best $SnO_2$ based DSSCs (about 2%) [52] and rank among the highest for $SnO_2$/ZnO composite photoanodes based DSSCs [48,51]. The $V_{oc}$ enhancement over that of the pure $SnO_2$ film is mainly responsible for the significant improvement in the overall efficiency of the $SnO_2$/ZnO composite film based DSSCs, since pure $SnO_2$ photoanode itself can also yield high photocurrent [52]. On the other hand, the difference in maximum efficiency among the three composite films is within 15%, which is mainly ascribed to the difference in $J_{sc}$. As another noteworthy feature, our composite photoanodes achieve the best performance at the weight ratio of $SnO_2$:ZnO = 2:1, and this contrasts with the work of Tennakone et al. on ZnO big particles/$SnO_2$ nanoparticles composite films, which obtained the maximum efficiency strictly at the ZnO:$SnO_2$ weight ratio of nearly 1:1 [42,51]. Such a difference is largely a result from the peculiar structure of our nanotetrapods, which possess three-dimensionally distributed long arms and can be embedded in the $SnO_2$ nanoparticles matrix without occupying much space in contrast to the space-filling, micron-sized ZnO particles used by Tennakone et al. [42,51].

### 3.3 Relationship between $J_{sc}$ and IPCE

To elucidate the dependence of the cell performance on the composition of our $SnO_2$/ZnO composite photoanodes, we analyzed the three determining factors of $J_{sc}$ and IPCE: $LHE(\lambda)$, $\Phi_{inj}$ and $\eta_{mL}$ [53]. Such analysis should be helpful for developing new composite photoanodes.

IPCEs of the three composite photoanodes are shown in Fig. 7. The maximum IPCE values are also selectively listed in Table 1. The maximum IPCE value for the three composite films at about 520 nm decreases from 74.1%, 71.5% to 67.6% with increasing content of ZnO nanotetrapods. As expected, this decreasing trend of IPCE for the composite films is naturally in keeping with the gradual drop of the maximum $J_{sc}$ from 16.3 $mA \cdot cm^{-2}$, 15.1 $mA \cdot cm^{-2}$ to 14.5 $mA \cdot cm^{-2}$ with increasing ZnO content. It is also important to recognize from Fig. 7 that with the increase of the ZnO content, the IPCE value in the long wavelength tail increases but suffers a comparable or higher decrease in the short wavelength region. A similar observation has also been reported on IPCE of a film in which a light scattering material was directly blended with $TiO_2$ nanoparticles [54].

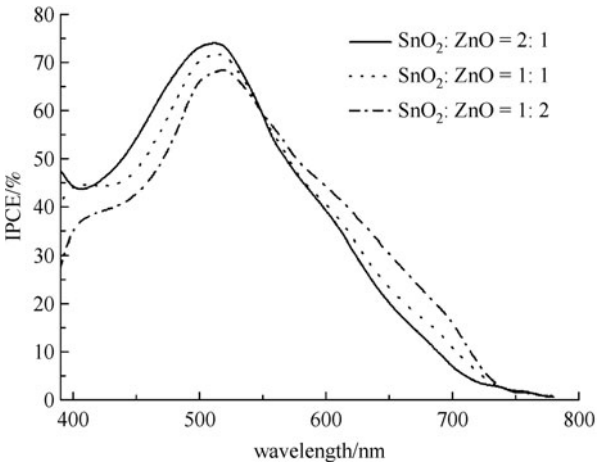


**Fig. 7** IPCE of DSSCs based on three typical composite photoanodes with different weight ratios as listed in Table 1 (Ref. [10], published with permission)

The *LHE* of a cell depends mainly on intrinsic properties of the dye, e.g., the wavelength dependent molar absorption coefficient, and its adsorbing density on porous photoanodes, which is governed by the Beer's law [50]. For a practical solar cell such as our ZnO nanotetrapods based DSSCs, the *LHE* equation should accommodate the scattering effect by introducing the concept of effective optical path length within the photoanodes. The effective optical path length can be increased by the addition of relatively large particles to small nanoparticles matrix to induce light scattering of the photoanodes, which is also called the light-trapping effect [49,55]. Such light trapping effect leading to enhancement on IPCE especially in the near-infrared wavelength range is very important for DSSCs, because the widely used Ru-pyridine based dyes absorb light weakly in this region. In our work, the broad pore size distribution resulted in relatively strong light scattering. As reflected in Fig. 4, the optical path length in the three composite films is gradually enhanced in the sequence of $SnO_2$:ZnO = 2:1, 1:1, and 1:2. Consequently, IPCE on the red side of the spectra is gradually enhanced in this sequence as revealed in Fig. 7.

To examine the difference in $\Phi_{inj}$, we employed the time-resolved fluorescence decay method [56,57] to probe the N719 dye in the three composite films with nearly the

**Table 1** Summary of performance parameters of DSSCs based on $SnO_2$ nanoparticles/ZnO nanotetrapods composite photoanodes

| sample | thickness/μm | $V_{oc}$/mV | $J_{sc}$/($mA \cdot cm^{-2}$) | *FF*/% | $IPCE_{max}$/% | $\eta$/% |
|---|---|---|---|---|---|---|
| $SnO_2$:ZnO = 2:1 | 6.6 | 656 | 16.3 | 0.59 | 74.1 | 6.31 |
| $SnO_2$:ZnO = 1:1 | 10.9 | 639 | 15.1 | 0.64 | 71.5 | 6.18 |
| $SnO_2$:ZnO = 1:2 | 13.5 | 648 | 14.5 | 0.62 | 67.6 | 5.83 |

same adsorbing amount. A pure N719 dye solution was used as a control. We observed that all of the three composite films yielded closely similar decay curves, which could be fitted with a biexponential model. Simply dividing the integral areas of the three fitted decay curves by that of the control, we could estimate the corresponding injection efficiencies, which were found to show negligible variations [10].

We next consider the charge collection efficiency, $\eta_{mL}$, determined by IMPS/IMVS measurements through the following equations [15,58,59],

$$\eta_{cc} = 1 - \frac{\tau_t}{\tau_r}, \tag{2}$$

$$\tau_t = \frac{1}{\omega_t} = \frac{1}{2\pi f_t}, \tag{3}$$

$$\tau_r = \frac{1}{\omega_r} = \frac{1}{2\pi f_r}, \tag{4}$$

where $\tau_t$, $\tau_r$ are electron transport time across the photoanode films and recombination time of electrons with $I_3^-$ ions in the electrolyte, respectively, and $f_t$ and $f_r$ are the characteristic frequency minimums of the IMPS and IMVS imaginary components, respectively.

Figure 8 plots $\tau_t$ and $\tau_r$ as a function of the incident photon flux (light intensity, $I_0$) for the three composite films. Obviously, the lower the content of ZnO nanotetrapods in a composite film, the larger the gap between $\tau_t$ and $\tau_r$, and thus the higher the change collection efficiency according to Eq. (2). More specifically, the charge collection efficiencies of the three composite films at the highest light intensity ($1.32 \times 10^{16}\,cm^{-2}\cdot s^{-1}$) are respectively 82.6%, 90.2%, and 95.0%, in the order of decreasing ZnO content. Such distinct differences in the charge collection efficiency is notably parallel to the composition dependent IPCE variations for the three composite films at 515 nm (the wavelength of the LED light source in IMPS/IMVS measurements), suggesting that $\eta_{mL}$ predominates *LHE* and $\Phi_{inj}$ in determining IPCE for the composite films. Such a charge collection limitation naturally explains the monotonic decrease of IPCE in the short wavelength region ($< 515$ nm) with the increase of ZnO nanotetrapod content (see Fig. 7). On the surface, the gradual decrease in charge collection efficiency with increasing ZnO content (resulting from the increase in charge transport time but the nearly constant recombination time) seems to be contrary to our expectation that more ZnO nanotetrapods should improve charge transport. However, for the same dye adsorbing amount and *RF*, photoinjected electrons need to transport a much longer distance (the film thickness) in the $SnO_2$:ZnO = 1:2 composite film to reach the conductive glass substrate than in the $SnO_2$:ZnO = 2:1 composite film.

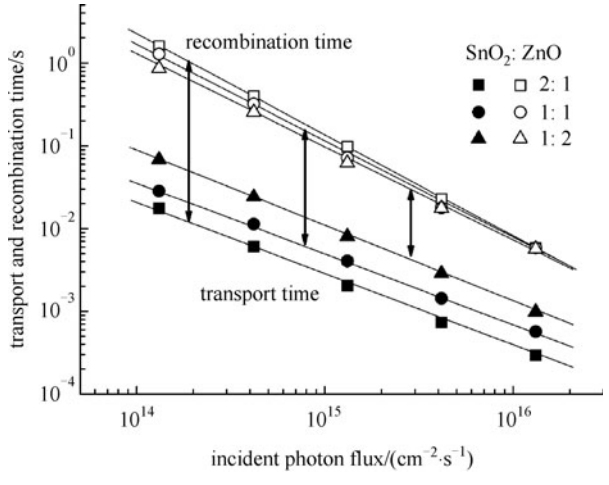


**Fig. 8** Incident light intensity dependent transport and recombination time constants for $SnO_2$ : ZnO nanotetrapods = 2 : 1, 1 : 1 and 1 : 2 composite photoanodes (as listed in Table 1) (Ref. [10], published with permission)

### 3.4 Role of ZnO naontetrapods on electron transport and recombination in the composite films

In the above, we have established that ZnO in the composite films exists in two forms: one is ZnO nanotetrapods and the other is ultrathin ZnO shells on $SnO_2$ nanoparticles. To clarify the roles of the ZnO nanotetrapods and the ZnO shells in charge transport and recombination kinetics in the composite films, we purposely dissolved ZnO in the composite films with acidic solutions while monitoring the charge transport and collection properties. For this study, the $SnO_2$:ZnO = 2:1 and 1:1 composite films were chosen and treated with 1% HAc in EtOH/$H_2O$ (1:2 by volume) for 30 min (denoted as sample HAc30) to totally dissolve ZnO nanotetrapods, resulting in nearly pure $SnO_2$ nanoparticles films. The structural differences between the original films and the corresponding HAc30 films have been confirmed by SEM and XPS. Corrosion of ZnO nanotetrapods yields new pore channels, leading to deteriorated continuity in the nanoparticles network. Figure 9 compares typical images of the $SnO_2$:ZnO = 1:1 composite film before and after HAc treatment, highlighting the corrosion induced porosity and the resulting discontinuity of the electron transport network. Such a scenario is definitely maintained in the $SnO_2$:ZnO = 2:1 composite film albeit to a less extent due to the lower ZnO nanotetrapods content. The differences between HAc treated films and their original films not only lie in the changed nanotetrapods' shape, but also relate to the altered ZnO shell thickness on $SnO_2$ nanoparticles which was revealed by XPS spectra in the core level region of Sn $3d_{5/2}$ of the original and HAc30 films [43].

It is of interest to pin down the extent to which ZnO nanotetrapods separately impinge on electron transport and recombination kinetics irrespective of the ZnO shell

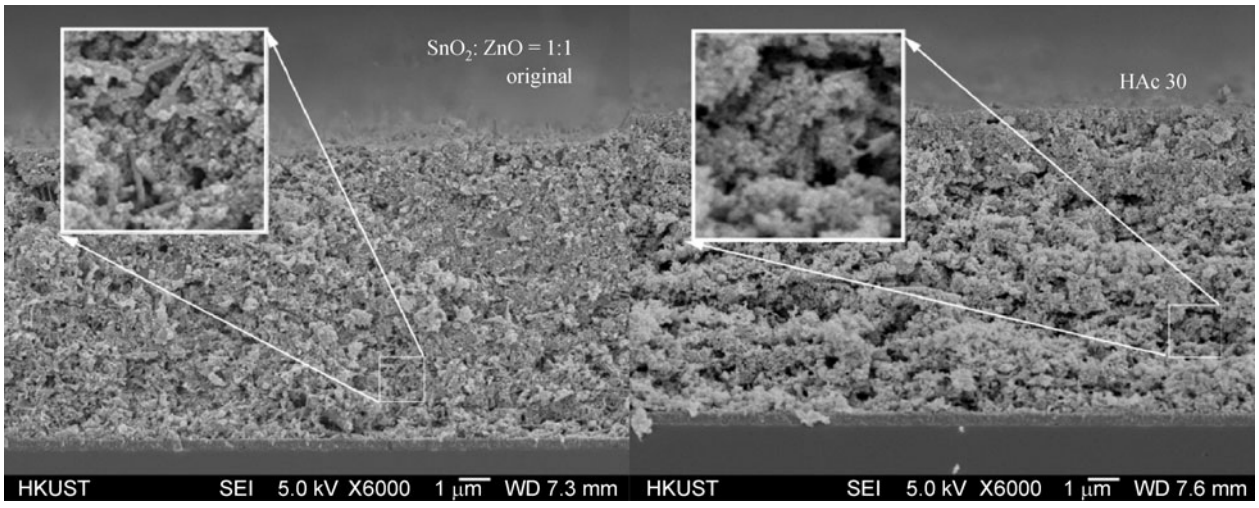


**Fig. 9** Cross section view SEM images showing structural differences between original $SnO_2$ : ZnO = 1 : 1 composite film (Original) and corresponding HAc30 film. Note that corrosion of ZnO nanotetrapods leads to more porous structure with less continuity in $SnO_2$ nanoparticles network (Ref. [10], published with permission)

thickness on $SnO_2$ nanoparticles, since both the corrosion of ZnO nanotetrapods and the decrease of the ZnO shell thickness occur simultaneously during the HAc treatment. So are the cell performance benefits from the structural advantages of ZnO nanotetrapods over ZnO particles in $SnO_2$/ZnO composite films [48,51]. Along this line, we opted to study two reference composite films (5.0±0.2 μm thick) prepared by blending our $SnO_2$ nanoparticles separately with two types of ZnO particles, one with a size of about 40 nm (synthesized according to Ref. [60].) and another with a size of about 500 nm (commercially available). The weight ratios of the two reference films were controlled at $SnO_2$:ZnO = 2:1 for the sake of comparison with the $SnO_2$:ZnO nanotetrapods = 2:1 composite film on transport and recombination kinetics. The large particles are similar to what were employed in literatures [48,51], while the small particles have a BET surface area of 25.6 $m^2 \cdot g^{-1}$, comparable to that of the ZnO nanotetrapods (BET = 18.9 $m^2 \cdot g^{-1}$), for which a similar dye adsorbing amount can be expected. Advantageously, because the ultrathin ZnO shells on $SnO_2$ are similar in all these films due to the similar preparation procedures used (this can also be appreciated from their similarly enhanced $V_{oc}$, all above 600 mV), the variation in transport kinetics can then be exclusively attributed to the changes of the ZnO particles or nanotetrapods in the composite films. To facilitate comparison, diffusion coefficient $D_n$ as an intrinsic material property will be used in place of $\tau_t$. It is calculated by $D_n \approx d^2/2.35\tau_t$ [15,61], where $d$ is the film thickness. According to the relationship between $D_n$ and $\tau_t$, the dependence of $D_n$ on light intensity ($I_0$) can also be described by a power law expression $D_n \propto (I_0)^{1-\alpha}$ [61].

$D_n$ and $\tau_r$ dependences on the incident photon flux (light intensity, $I_0$) of the composite films are shown in Figs. 10 (a) and 10(b). Taken as a whole, Fig. 10(a) highlights the importance of morphologies of the ZnO additives in modulating the transport kinetics given the similar ZnO shelled $SnO_2$ nanoparticles for all of the composite films, while Fig. 10(b) repudiates any substantial influence of such morphologies on the recombination kinetics, leaving behind the ultrathin ZnO shells on the $SnO_2$ nanoparticles as the main determinant of recombination kinetics in the composite films. In getting into more details, we attend to a few important features in Fig. 10(a). First, $D_n$ of the ZnO nanotetrapods derived composite film is larger than those of the two reference films, especially that of the small ZnO particles reference film by a factor of 2.18 to 3.72 in the tested light intensity range. Second, the logarithmic slope $(1-\alpha)$ of $D_n$ dependence on $I_0$ for the ZnO nanotetrapods derived composite film ($\alpha = 0.11$) is much larger than those for the reference composite films ($\alpha = 0.27$ for the small ZnO particles reference film; $\alpha = 0.41$ for the big ZnO particles reference film, $\alpha = 0.41$). Third, $D_n$ for the small ZnO particles reference film is smaller than that of its corresponding HAc30 film, in marked contrast to the fact that $D_n$ for the ZnO nanotetrapods derived composite film is mostly larger than that of its corresponding HAc30 film.

The larger $D_n$ value and the larger logarithmic slope of $D_n$ dependence on light intensity for the ZnO nanotetrapods derived composite film are testament of the more efficient charge collection than for the two ZnO particles reference films, which become even more apparent under closer to 1 sun light illumination (the highest light intensity employed in our IMPS/IMVS study was only about 1/20 sun). This is consistent with our experimental observation that, under similar film fabrication and solar cell test conditions, the cell performance for the ZnO particles derived composite films proved to be inferior to that for our ZnO nanotetrapods/$SnO_2$ nanoparticles composite films.

The sharp contrast between the HAc-induced increase of

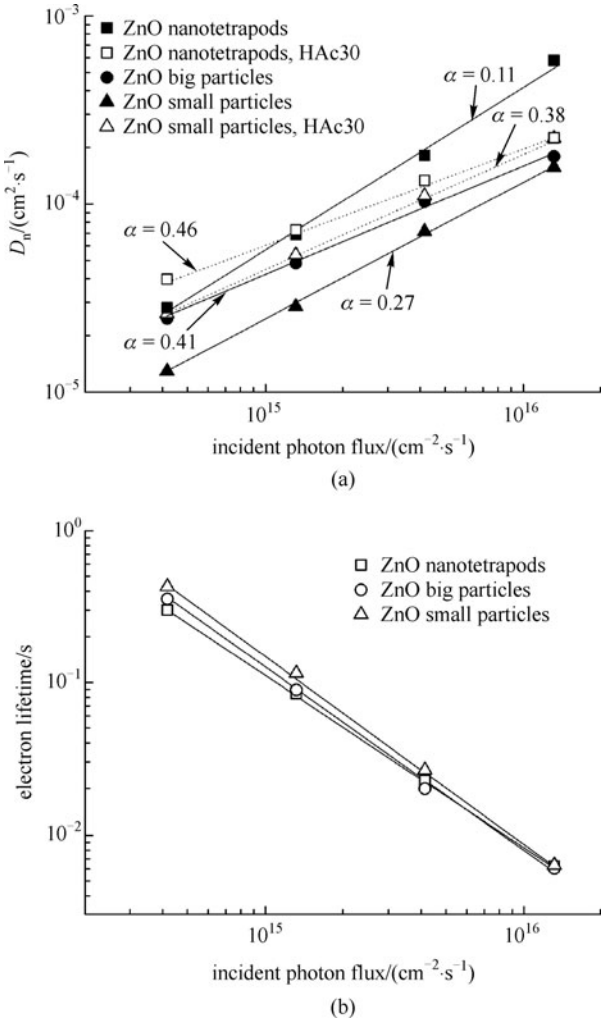


**Fig. 10** Incident light intensity dependent electron diffusion coefficient $D_n$ (a) and electron lifetime $\tau_r$ (b) of the $SnO_2$ : ZnO nanotetrapods = 2 : 1 composite film and two reference films with the ZnO nanotetrapods being replaced by ZnO small particles (40 nm) or ZnO big particles (500 nm). Straight lines represent power-law fits. $\alpha$ values are calculated from logarithmic slopes (1-$\alpha$) by least square fitting (Ref. [10], published with permission)

$D_n$ for the small ZnO particles reference film and the HAc-induced decrease of $D_n$ for the ZnO nanotetrapods derived composite film accentuates the "high-way" role of the nanotetrapods and connotes a "relay transport" mechanism in the composite films. In the "relay transport" scenario, photoinjected electrons are free to move from $SnO_2$ nanoparticle regions to ZnO additive regions, and vice versa, and finally reach the conductive glass substrate, contributing to the overall $J_{sc}$ of the solar cell. If only the unidirectional electron injection from ZnO part to the $SnO_2$ nanoparticles matrix were allowed but not the reverse, $D_n$ values of the composite films should not have shifted toward the antithetic directions upon the HAc treatment just because of different morphologies of the ZnO additives. Plausibly, the more numerous grain boundaries between small ZnO particles and $SnO_2$ nanoparticles would mean more electron traps [39], which would contribute more to the impediment to the inter-particle electron transport. Hence the dissolution of ZnO by HAc should result in increase of $D_n$ as observed. On the other hand, in the ZnO nanotetrapods derived composite film, the ZnO-$SnO_2$ grain boundaries are much reduced and the ZnO nanotetrapods figure prominently in the electron transport. As a result, the HAc-induced ZnO dissolution led to the decrease of $D_n$.

As regards the recombination kinetics in the composite films, the similar ZnO shells on $SnO_2$ play the major role instead of the morphology of ZnO crystalline additives since the amount of dye taken up by ZnO crystalline additives is much smaller than that by $SnO_2$ nanoparticles for all the three composite films. Furthermore, for recombination, photoinjected electrons only need to diffuse to the outer surfaces of nanoparticles (particles) or nanotetrapods, hence the effect of the grain boundaries mentioned above is much less consequential as evidenced by the similar recombination kinetics in Fig. 10(b) for the different ZnO-$SnO_2$ composite films.

## 4 ZnO nanotetrapod based flexible DSSCs

In view of the prima facia advantages of ZnO nanotetrapods such as fast electron transport and network-forming ability, we have explored their use in flexible DSSCs. An effective low temperature fabrication technique of "acetic acid gelation-mechanical press-ammonia activation" (hereafter denoted as "AG-MP-NA") has been developed to deposit the $SnO_2$ nanoparticles/ZnO nanotetrapods composite film on a conductive plastic substrate, scoring a cell efficiency of 4.91%. Several novel features of the method can be summarized here: 1) The in situ formation of ZnO shell on $SnO_2$ nanoparticles in a composite film plus the key HAc gelation and $NH_3$ activation steps cannot only raise open-circuit photovoltage ($V_{oc} \approx 700$ mV) with respect to pure $SnO_2$ based DSSCs (no more than 400 mV [43]) but also consolidate physical and electrical contacts between $SnO_2$ nanoparticles; 2) the 1D arms of ZnO nanotetrapods dispersed in the $SnO_2$ nanoparticles matrix can minimize grain boundaries, facilitate directed charge transport and improve charge collection just as we have demonstrated above in high temperature calcined $SnO_2$ nanoparticles/ZnO nanotetrapods composite photoanodes [10,11]; 3) the branching structure of the nanotetrapods makes it apt to form network structures on flexible substrate with good mechanical durability, which can be processed further by mechanical press.

We start by illustrating the "AG-MP-NA" method in Fig. 11. The corresponding composite film morphologies at different stages of the operation are revealed by the SEM images in Fig. 12. Associated with step 1 is the initial

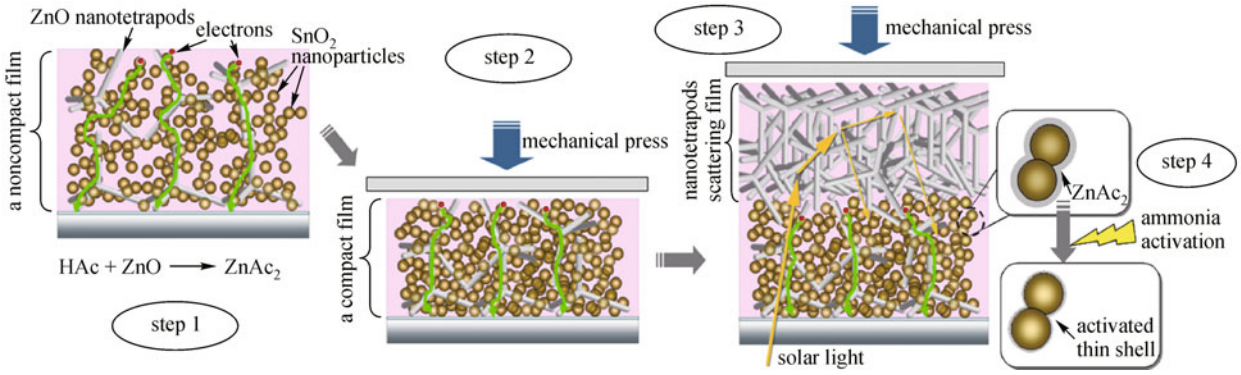


**Fig. 11** Schematic showing low temperature technique of "AG-MP-NA" and its effects on films' morphology, surface condition, as well as resulting electron transport and light scattering properties (Ref. [11], published with permission)

spreading of a $SnO_2$ nanoparticles/ZnO nanotetrapods paste onto an FTO-coated glass or ITO/PEN flexible substrate (Figs. 12(a)–12(c)). Diluted HAc was included in the paste to partially corrode the ZnO nanotetrapods, promoting the formation of a zinc acetate ($ZnAc_2$) shell layer on the $SnO_2$ nanoparticles. The as-deposited film from random stacking of the binary nanomaterials contains interspaces between nanotetrapods not fully filled by nanoparticles, making the freshly deposited film look rather hollow with low connectivity (Figs. 12(b), 12(c)). In step 2, an 80–100 MPa hydraulic pressure was applied to the freshly deposited film. As a result, the film thickness is decreased by nearly half (Figs. 12(a), 12(d)), and the $SnO_2$ nanoparticles and ZnO nanotetrapods in the film become much more densely stacked (Figs. 12(e), 12(f)). Conceivably, the transport pathways of photoinjected electrons in the pressed film should be much shorter than those in the unpressed ones as denoted by the green arrow-lines in Fig. 11. More to the point, close packing may imply better contacts between nanostructures in the composite film as well as between the active film and the conductive substrate. For example, the large pores (interspaces) seen in the unpressed film have been filled and/or eliminated by pressing. Step 3 begins with the deposition of another layer but made of pure ZnO nanotetrapods on top of the $SnO_2$/ZnO composite film (Fig. 12(h)). After mechanical press, a dense, robust network is formed (Fig. 12(i)). The compression ratio for this layer is about 4, namely, from 12 to 13 to 3.3 μm (Fig. 12(g)). Its *RF* (total inner pore surface area dived by active film area) is about 150–200, according to our previous work [7], which is about 1/8–1/6 that of the under-layer composite film ($RF \approx 1200$ by multiplying BET surface area of 65.3 $m^2 \cdot g^{-1}$ to the weight of 1 $cm^2$ area film). The main function of this layer, aside from the light absorption, lies in the light scattering in the near-infrared region. Its light scattering capability is derived from the sub-micron level pores formed of the nanotetrapods [29]. The inimitable branching structure of our nanotetrapods has imparted this light scattering a certain extent of toughness to endure curvature bending on flexible substrates, a distinct advantage over other kinds of light-scattering materials such as large $TiO_2$ particle assemblies and $SiO_2$ sphere photonic-crystals previously applied to DSSCs [62]. In the last step, the pressed film is immersed in 0.3 M $NH_3$ solution for 20 min and then kept at 150°C for 30 min. This procedure is intended to wash away the unwanted zinc acetate ($ZnAc_2$) on $SnO_2$ and promote the formation of an ultrathin ZnO shell firmly attached to $SnO_2$, the effectiveness of which has been demonstrated by infrared spectra of the films before and after $NH_3$ treatment. Such a shell is important not only for better inter-particles connections, but also for boosting $V_{oc}$ of the $SnO_2$/ZnO composite film based DSSCs by elevating the conductive band edge of $SnO_2$ toward that of ZnO, as revealed in previous works [10,43].

Diffuse reflectance spectroscopy was used to track the changes of light scattering property due to the treatment-induced changes in pore structure [11]. For low temperature treaded films, owing to the no use of binder in the film-preparation paste normally added for releasing the capillary force between nano-constituents, the structural incompatibility between the nanotetrapods and the nanoparticles was more serious. Therefore the as–deposited thick film before mechanical press was loosely stacked. Its open pore structure rendered a large fraction of visible light being multiply scattered. After mechanical press, however, the film becomes translucent because the large pores as the light scattering centers are mostly eliminated. This is in keeping with the diffuse reflectance spectrum of the film with significantly reduced multiple light scattering in the visible region. By overlaying a top layer of pure ZnO nanotetrapods, the film becomes totally opaque. The corresponding diffuse reflectance spectrum confirms that multiple light scattering in this film is the strongest of the three.

Shown in Fig. 13(a) are photocurrent density-voltage (*J-V*) characteristic curves of representative DSSCs based on the single layer composite film (Fig. 12(d)) and double-layer-structured film (Fig. 12(g)) on FTO-coated glass and on ITO/PEN substrates. The insets in Fig. 13(a) are optical

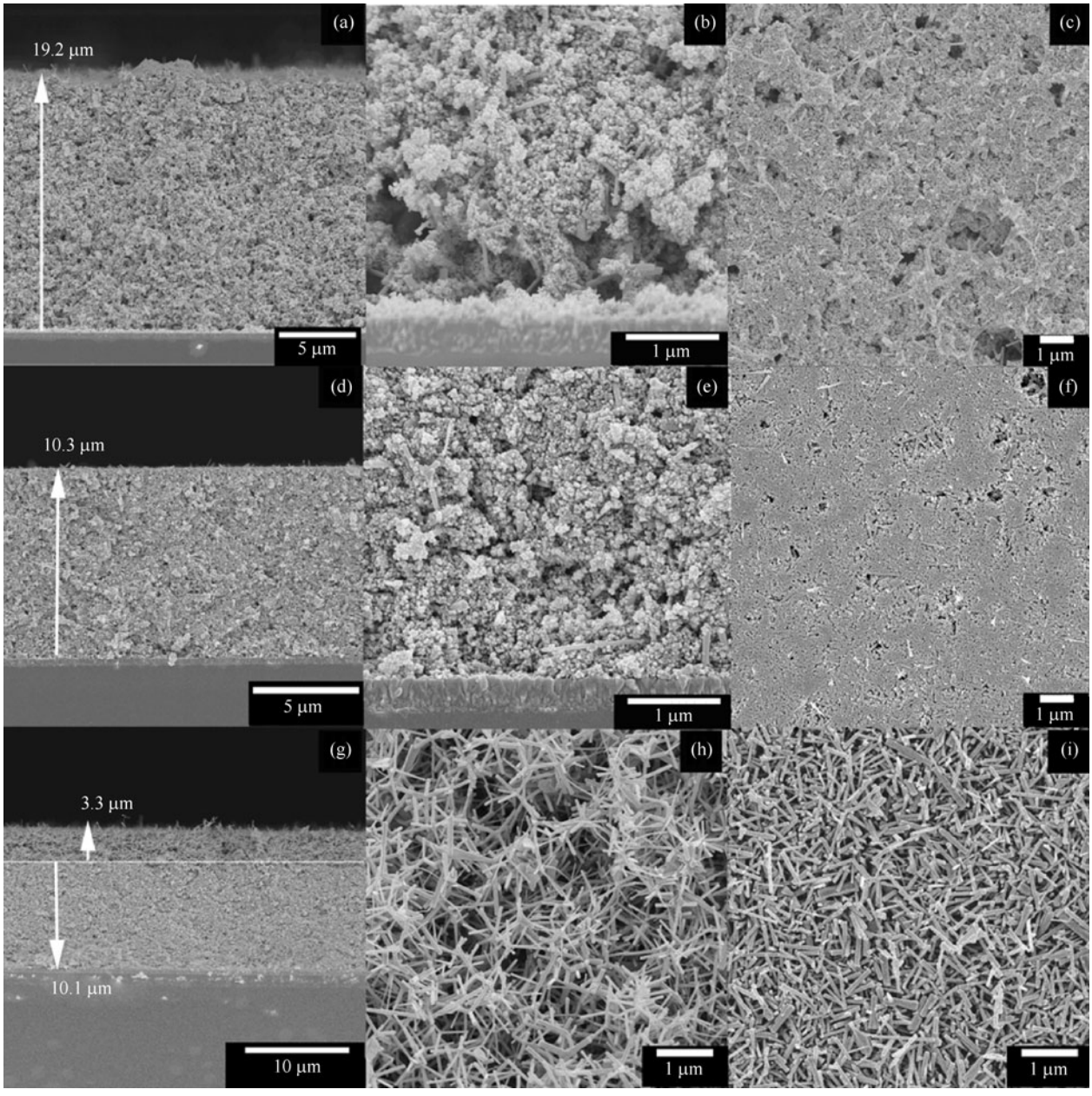


**Fig. 12** SEM images of single-layer composite film before (a)–(c), after pressing procedure (d)–(f), and a double-layer-structured film (g)–(i). (a), (d) cross-section view: film thickness is decreased from 19.2 to 10.3 μm due to pressing procedure; (b), (e) cross-section view highlighting difference at active film/FTO-coated glass interface; (c), (f) top view showing different porosities; (g) cross-section view: top light scattering layer is 3.3 μm thick ZnO nanotetrapods network; (h), (i) top view showing the different packing densities of nanotetrapods before (h) and after pressing procedure (i) (Ref. [11], published with permission)

images of the corresponding dye sensitized films. The dark red color reflects sufficient dye adsorbing amount which was detected to be $1.47 \times 10^{-7}$ mol·cm$^{-2}$ at the roughness of about 1200 for the single layer film on FTO-coated glass. Double layer film possesses $1.72 \times 10^{-7}$ mol·cm$^{-2}$ dye adsorbing amount at the total *RF* of about 1400 on FTO-coated glass. High bending curvature images of the two films on flexible substrates indicate good mechanical adhesion, another benefit of the pressing procedure and the branching structure of nanotetrapods. This is rather similar to the case of material strengthening arising from fibrous reinforcement. The performance parameters of the DSSCs are listed in Table 2. Notably, our 4.91% efficiency at 1 sun on TCP substrate is among the highest of low temperature processed flexible photoanodes [16,23,63–65] and the $V_{oc}$ is even about 50 mV higher than that of the calcined $SnO_2$ nanoparticles/ZnO nanotetrapods composite photoanode we reported previously [10]. The improved $V_{oc}$ is mainly

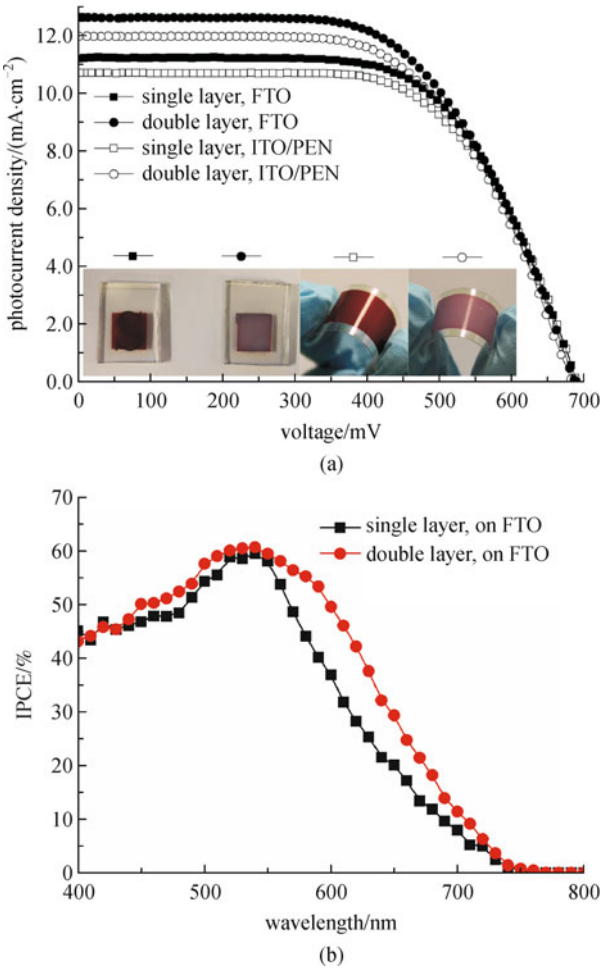


**Fig. 13** (a) *J-V* characteristic curves of DSSCs based on "AG-MP-NA" processed films on FTO-coated glasses (solid symbols) and ITO/PEN flexible substrates (open symbols) (inset show photographs of dye sensitized films used to record *J-V* curves, from left to right, single-layer composite film (■) and double-layer-structured film (●) on FTO-coated glasses, and single-layer composite film (□) and double-layer-structured film (○) on flexible substrates); (b) IPCE spectra of DSSCs based on single-layer composite film and double-layer structured film on FTO-coated glasses in (a) (Ref. [11], published with permission)

**Table 2** Performance parameters of best performance DSSCs on FTO-coated glasses (S1: single layer, D1: double layer) or ITO/PEN flexible substrates (S2: single layer, D2: double layer), corresponding to *J-V* characteristic curves in Fig. 13(a)

| samples | $V_{oc}$/mV | $J_{sc}$/(mA·cm$^{-2}$) | *FF*/% | efficiency/% |
|---|---|---|---|---|
| S1 | 692 | 11.2 | 0.63 | 4.87 |
| D1 | 688 | 12.6 | 0.59 | 5.16 |
| S2 | 690 | 10.7 | 0.63 | 4.65 |
| D2 | 684 | 12.0 | 0.60 | 4.91 |

ascribed to the employment of ammonium iodide ($NH_4I$) based electrolyte instead of imidazolium iodide. While the imidazolium iodide based electrolyte is traditionally optimized with respect to $TiO_2$ photoanodes, the $NH_4I$ based electrolyte appears to be more compatible with ZnO based DSSCs [32,66], presumably due to the favorable adsorption of $NH_3/NH_4^+$ on ZnO surfaces and therefore the suppression of recombination kinetics. This can be appreciated from our electrochemical impedance results on $SnO_2$ nanoparticles/ZnO nanotetrapods composite films with the two different electrolytes: the recombination time is 40% longer in the $NH_4I$ based electrolyte. In comparison to the record $TiO_2$ nanoparticles photoanode on TCP substrate (with 7.4% efficiency), the relatively low efficiency of our composite photoanode is mainly due to the lower short-circuit photocurrent density ($J_{sc}$, 12.0 versus 13.4 mA·cm$^{-2}$) and fill factor (*FF*, 0.60 versus 0.74) [16]. These performance gaps could be further narrow down by optimizing the nanostructures of our composite photoanode and employing better quality plastic conductive films. It is clear that double-layer-structured films possess notably higher $J_{sc}$ but slightly decreased $V_{oc}$ and *FF* in comparison with their corresponding single layer $SnO_2$ nanoparticles/ZnO nanotetrapods composite films. Plausibly, the higher $J_{sc}$ is mostly due to light scattering enhanced IPCE in the near-infrared region, which has been confirmed in Fig. 13(b). The slight decrease of $V_{oc}$ and *FF* is likely due to the addition of the ZnO nanotetrapods scattering layer, which could modify series resistance and shunt resistance as well as their relationship in the whole film. A larger series resistance and lower shunt resistance for the double layer film than the single layer film can be clearly revealed by their different impedance spectra. According to the well documented one–diode model for DSSCs [3,53,67,68], such changes will lead to smaller $V_{oc}$ and *FF*, a result we have presented above. The relatively better performance of FTO-coated glass than that of ITO/PEN flexible substrate based DSSC is primarily due to the lower transmittance of the ITO/PEN substrate than the FTO-coated glass used in our experiment.

Figure 14 compares typical *J-V* curves (Fig. 14(a)), EIS (Fig. 14(b)) and charge collection kinetics (Fig. 14(c), studied by IMPS/IMVS) of a composite film at different steps of the "AG-MP-NA" technique. Clearly identified are effects of the mechanical press and $NH_3$ activation steps on the electrical and charge collection properties of the film tied up with the cell performance (Table 3). Here we use "HAc, unpressed film" and "HAc-$NH_3$, unpressed film" to denote the as-deposited unpressed composite films (about 12 μm thick) with and without $NH_3$ treatment, respectively. "HAc-$NH_3$, pressed film" represents the film that has been through the complete procedure including both mechanical press and $NH_3$ activation treatment. After pressing, the "HAc-$NH_3$, pressed film" is thinned to about 6.5 μm. We first compare the "HAc-$NH_3$, unpressed film" with the "HAc-$NH_3$, pressed film" to establish the effect of the

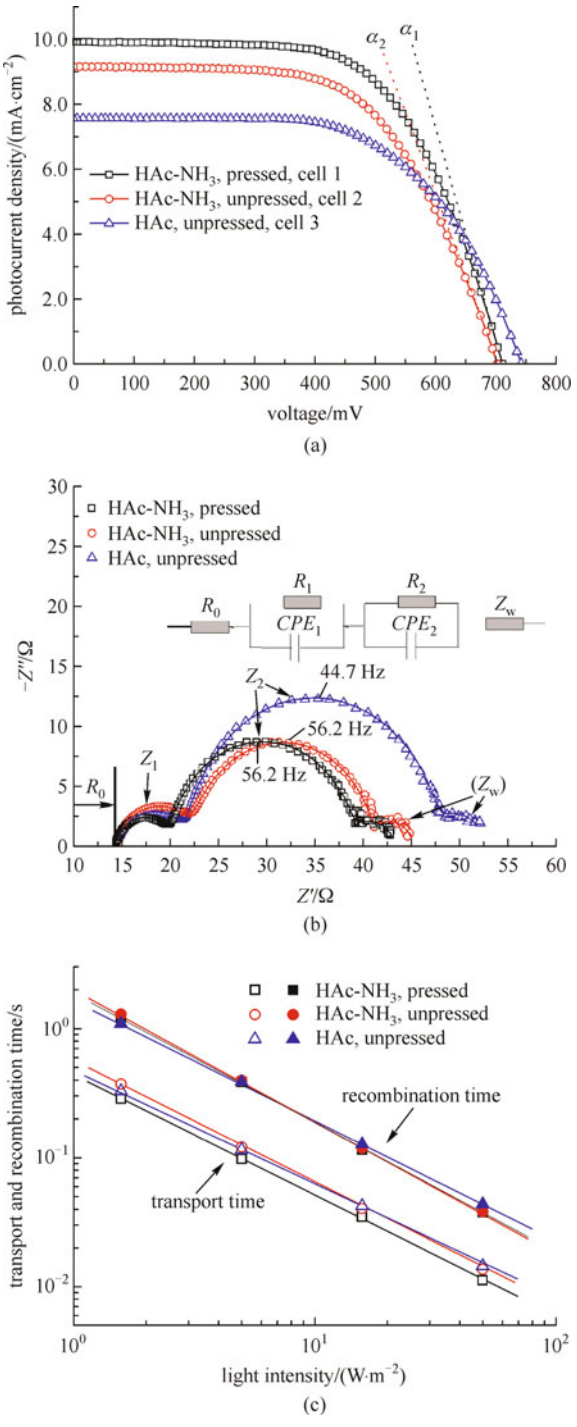


**Fig. 14** (a) *J-V* characteristic curves of composite films: black square, film treated by pressing and $NH_3$ activation (film thickness $\approx$ 6.5 μm, cell 1); red circle, film treated by $NH_3$ activation but without pressing (film thickness $\approx$ 12 μm, cell 2); blue up-triangle, as-deposited film without further treatment (cell 3). $\alpha_1$ and $\alpha_2$ highlight different slopes of the tangents at the open-circuit voltage; (b) EIS Nyquist plots from impedance spectra of the films together with the fitted results (solid line) based on the equivalent circuit model as shown in inset; (c) electron transport and recombination times of the films from IMPS/IMVS measurements. Straight lines are fitted results (Ref. [11], published with permission)

pressing procedure. From Fig. 14(a), it can be observed that in comparison to the "HAc-$NH_3$, unpressed film," all parameters including $J_{sc}$, $V_{oc}$ and *FF* of the "HAc-$NH_3$, pressed film" have been improved, and the efficiency has been steadily improved by about 13%, from 3.85% to 4.35%.

It should be noticed that the impedance spectra in Fig. 14(b) were recorded under 1 sun illumination and at open circuit potential, a condition which is quite different from that in Fig. 3. Correspondingly, a different equivalent circuit model should be applied. We employed a model (see the top inset in Fig. 14(b)) similar to those used previously by other researchers [34,35] to fit our EIS results. It can be seen that the left arc in the high frequency range ($10^4 - 10^2$ Hz) shrivels evidently due to mechanical press. This arc, denoted as impedance $Z_1$, is associated with charge transport at FTO/active film, Pt/electrolyte, as well as inter-nanostructure interfaces. No matter which of these interfaces is tied to such mechanical press induced arc-shrinking, the mechanical press generally reduces the total series resistance ($R_s$) of the cell. According to the one-diode model of solar cell [33], a smaller $R_s$ commonly gives rise to a higher *FF* [53,68], which is also echoed by the tangential slopes (denoted as $\alpha_1$ and $\alpha_2$) at the open-circuit voltages of the *J-V* curves. The scenario is in concurrence with the results in Fig. 14(a) and in Table 3. The middle arcs in Fig. 14(b) (denoted as $Z_2$, recombination resistance $R_2$ in parallel with $CPE_2$, on the frequency scale of about $10^1$ Hz), which arise from charge recombination at the active film/electrolyte interface, appear to have no direct causality with the pressing procedure; their fitted $R_2$ and characteristic frequency $f_2$ changed little. Charge collection efficiencies ($\eta_{mL}$) of the films before and after mechanical press were investigated by measuring the characteristic frequencies ($f_t$ and $f_r$) using IMPS and IMVS, respectively, and then calculated by using Eqs. (2)–(4). As one can see from Fig. 14(c), there are obvious gaps in $\tau_t$ between films with and without mechanical press, whereas their $\tau_r$ are very similar, in agreement with the result of EIS presented above. The faster electron transport in a thinner pressed film, due mainly to a shorter electron transport pathway as illustrated in Fig. 11, has led to an enhanced charge collection efficiency, from 64% to 70%, determined by using the data (at the light intensity of 50 W·m$^{-2}$) in Fig. 14(c). Such decent improvement of $\eta_{mL}$ appears to be main cause for the increase of $J_{sc}$ as described in Fig. 14(a) resulting from the pressing procedure.

**Table 3** Performance parameters of DSSCs corresponding to *J-V* characteristic curves in Fig. 13(a)

| samples | $V_{oc}$/mV | $J_{sc}$/(mA·cm$^{-2}$) | *FF*/% | efficiency/% |
|---|---|---|---|---|
| cell 1 | 712 | 9.9 | 0.62 | 4.35 |
| cell 2 | 703 | 9.1 | 0.60 | 3.85 |
| cell 3 | 743 | 7.6 | 0.60 | 3.38 |

The role of $NH_3$ treatment is mainly to activate the nanostructured surface, which is important in balancing the transport/recombination kinetics, but more critical appears to be to modulate the injection quantum efficiency for enhancing the cell performance. This point is supported by our new evidence obtained from EIS and IMPS/IMVS. In comparing the impedance spectrum (Nyquist plot) of "HAc, unpressed film" with those of the other two films treated by $NH_3$ (Fig. 14(b)), one notices a significant larger middle arc associated with electron recombination at the active film/electrolyte interface. The characteristic frequency ($f_2$, frequency corresponding to the maximum $|Z'|$ point of the middle arc) equals to 44.7 Hz, which is evidently lower than those of the other two films (56.2 Hz). This implies that under the test conditions for impedance spectroscopy, i.e., at 1 sun light intensity, the recombination time of "HAc, unpressed film" is much longer than those of the other two films, simply judging from $\tau_r = 1/(2\pi f_2)$. This result tallies with the corresponding IMVS data shown in Fig. 14(c): at higher light intensity in the tested range (from 1.58 to 50 $W \cdot m^{-2}$), $\tau_r$ of "HAc, unpressed film" becomes gradually longer than those of the other two films. The larger recombination resistance ($R_2$) and longer recombination time ($\tau_r$) strongly suggest different surface properties of the film without $NH_3$ treatment. In principle, such changes can be ascribed to the unwanted ZnO precursors in the non-$NH_3$-treated film. The unwanted ZnO precursors could promote the formation of Zn-dye complexes during the dye-adsorbing process, which could hang on the surfaces of the nanostructures and act as an insulating layer, blocking the back reaction pathway of photoinjected electrons from semiconductors to electrolyte. That could be the reason why $V_{oc}$ of such non-$NH_3$-treated film ($V_{oc}$ = 743 mV) is even higher than those of the other two films ($V_{oc}$ = 712 – 703 mV, Table 3). Another noteworthy aspect for the "HAc, unpressed film" is that, its calculated charge collection efficiency ($\eta_{mL}$) equals to 67% at 50 $W \cdot m^{-2}$, which is even higher than that of "HAc-$NH_3$, unpressed film" ($\eta_{mL}$ = 64%), whereas its $J_{sc}$ is much lower. Such abnormality implies that there should be other limiting factors responsible for such low $J_{sc}$. *LHE* is determined by dye adsorbing amount and light-scattering-corrected optical length of a photoanode film. We suggest that *LHE* should not be influenced much by the $NH_3$ treatment and thus cannot be responsible for the $J_{sc}$ gap mentioned above, because of no detectable difference in the dye adsorbing amount and light scattering property. The only remaining factor is $\Phi_{inj}$ of the non-$NH_3$-treated film, which can be low due to the presence of the Zn-dye complexes as discussed in the last section and in Ref. [30].

Figure 15 examines the effect of ZnO nanostructural morphologies (nanotetrapods and big particles about 500 nm in size) on charge collection efficiencies of the $SnO_2$/ZnO nanocomposite photoanodes and the resulting cell performance of the corresponding DSSCs. For comparison on the same footing, we used the same weight ratios of $SnO_2$/ZnO and treatments throughout the experiments. Apparently from Fig. 15, the improvements of $\eta_{mL}$ by > 10% for the ZnO nanotetrapods over the ZnO big particles should be mostly ascribed to the enhancement of $J_{sc}$, due to the structural superiority of the ZnO nanotetrapods to the ZnO big particles. Referring to the high temperature calcined $SnO_2$/ZnO composite films based DSSCs we studied previously [10], the ZnO crystalline additives in the composite films should similarly play two functional roles in the "AG-MP-NA" treated films because similar features of electron transport and recombination kinetics have been found: a) they act as a Zn source for forming a ZnO shell on $SnO_2$ nanoparticles; b) depending on their morphologies, they impact greatly on the electron transport kinetics in composite films. Namely, ZnO additives can locally gather electrons from the neighboring $SnO_2$ nanoparticles and promote fast electron transport due to ZnO's higher electron mobility (see the green arrow-lines in Fig. 11). Fundamentally, the fact that ZnO nanotetrapods support faster electron transport in composite films than ZnO big particles can be ascribed to their structural difference: the big ZnO particles are a space-filling object, whereas the ZnO nanotetrapods are a branched one dimensional (1D) material: its 1D arms ensure facile directional charge transport and its symmetric branching structure guarantees good network forming ability and optimized contacts between the binary constituents in composite films. From the SEM images shown in Fig. 16, we can easily estimate the average distance for photogenerated electrons in $SnO_2$ nanoparticles to migrate and make their way into the nearest neighboring ZnO crystalline additives for the

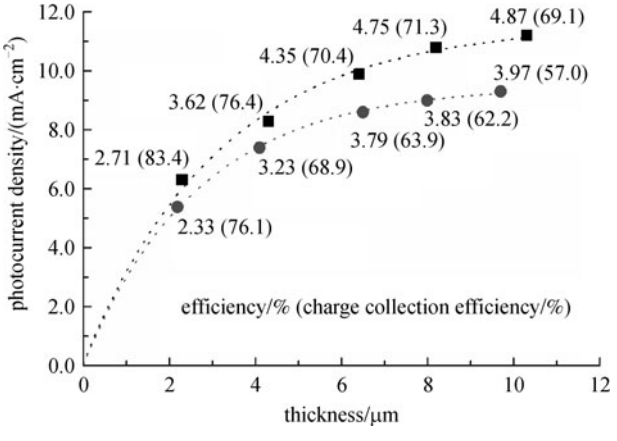


**Fig. 15** Dependences of $J_{sc}$ and efficiency (charge collection efficiency) on film thickness for two kinds of nanocomposite films on FTO-coated glasses: black square, $SnO_2$ nanoparticles/ZnO nanotetrapods; red circle, $SnO_2$ nanoparticles/ZnO big particles. Charge collection efficiencies were calculated from data measured by IMPS/IMVS at 70 $W \cdot m^{-2}$ (Ref. [11], published with permission)

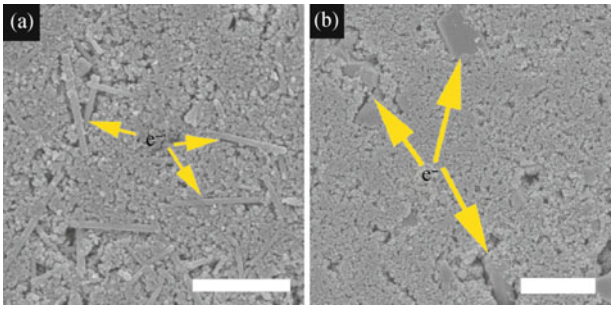


**Fig. 16** SEM images of composite films containing ZnO nanotetrapods (a) and ZnO big particles (b) as additives. Scale bar = 1 μm. Yellow arrow-lines highlight different lengths the localized electrons have to migrate from $SnO_2$ nanoparticles to neighboring ZnO sites (Ref. [11], published with permission)

subsequent accelerated transport in ZnO. For ZnO nanotetrapods, such distance is a few hundred nanometers; whereas it is dramatically increased to several microns for ZnO big particles, as highlighted by the yellow arrows.

## 5 Conclusions

In the work reviewed here, we have systematically studied the use of ZnO nanotetrapods for DSSC photoanodes, More specifically, we have realized a novel photoanode architecture based on pure ZnO nanotetrapods and demonstrated its outstanding charge collection property. For such ZnO nanotetrapod photoanodes with film thickness up to $> 30$ μm, the corresponding DSSCs exhibit high $V_{oc}$ and high *FF* even without calcination. $J_{sc}$ increases to 10.31 $mA \cdot cm^{-2}$, and the efficiency has reached 3.27%. The unique features of thick photoanode and no calcination make our ZnO nanotetrapod photoanodes especially distinct from most of the nanoparticle photoanodes reported to date.

In another significant stride, we were able to boost the efficiency to 6.31% by blending the ZnO nanotetrapods with $SnO_2$ nanoparticles. For composite films with higher ZnO nanotetrapods contents, due to the requirement of higher film thicknesses, charge collection losses appear to be a main limiting factor which compromises the benefit from their favorable light scattering ability. We have shown that a ZnO source, be it from particles or nanotetrapods, tends to form a generally similar ultrathin ZnO shell on $SnO_2$ nanoparticles. By comparison studies using the IMPS/IMVS technique, the functional roles of the ultrathin ZnO shell and the ZnO nanotetrapods in the $SnO_2$/ZnO composite film have been further elucidated: 1) The ultrathin ZnO shell mainly determines the recombination kinetics rather than the transport rate in the composite films; 2) ZnO nanotetrapods contribute to electron transport in composite photoanodes most probably in a "relay transport" manner, and due to the minimal to moderate hetero-particle grain boundaries, electron transport kinetics is facilitated in the ZnO nanotetrapods derived composite film, accentuating the structural and thus transport supremacy of our branched nanostructure over particles additives in the $SnO_2$/ZnO composite photoanodes.

The next march was the demonstration of applying the ZnO nanotetrapods to flexible DSSCs for the first time. A 4.91% efficiency has been achieved with a $SnO_2$ nanoparticles/ZnO nanotetrapods composite photoanode on a plastic substrate. The use of these special nanostructures led to the development of a low temperature technique of "AG-MP-NA," which has proved effective for activating nanostructured surfaces (better electron injection), shortening electron transport pathways (better charge collection), and ultimately improving cell performance. Two unique characteristics of this nanocomposite photoanode design have rendered it applicable to flexible DSSCs. First, the ZnO shell on $SnO_2$, conducive to good contacts between nanoparticles and $V_{oc}$ enhancement, is easily activated under a mild condition of $NH_3$ treatment. Second, the ZnO nanotetrapods with a symmetrically branching 1D structure not only ensures facile network formation on flexible substrate with good mechanical durability, further enhanced by mechanical press, but also has positive bearing on electron transport resulting in an improved charge collection efficiency when compared with ZnO big particles. To sum up, this work points to a promising alternative direction for the development of flexible solar cells by exploiting the core-shell, branching and composite nanostructures.

As often happens, our studies also left many questions unanswered. For example, it is unclear why the *FF* increases with film thickness. Does the nanotetrapod network need a different charge transport modeling approach? Moreover, we need a more detailed understanding about how the photoexcited electrons are injected from $SnO_2$ to ZnO. How do the material combination and the interface structure influence the interfacial charge transfer? Therefore it goes without saying that more work is needed to further understand the transport and optical properties of the ZnO nanotetrapods networks. In terms of DSSC device, although we have achieved reasonable efficiencies, there are still problems of charge collection, especially for the composite system on flexible substrates, for which low temperature treatments are the rule. In particular, the electron transport in low-temperature treated photoanodes is slower than in calcined ones. The solution to this problem will rely on the further development of the bottom-up nanotechnology.

Looking ahead, further improvements on the cell performance of the composite photoanodes can be anticipated by taking on several lines of investigation. First, the ZnO nanotetrapods should be grown with thinner diameters and longer arms so as to enhance surface area and improve the connectivity of the network. Second, new

film deposition methods need be developed to improve the electrical contacts between the nanotetrapods and the conformity between the nanotetrapods and the embedded nanoparticles. One way is to first build a firmly connected ZnO nanotetrapods network as the electron transport highway, and then deposit the small $SnO_2$ nanoparticles or ZnO nanoparticles penetrating into and fully filling the remaining spaces. The latter can be accomplished by electrophoretic deposition, which has been widely applied in photoanode film deposition in flexible DSSCs [69,70]. Third, a thin uniform coating of, e.g., $TiO_2$, onto the ZnO nanotetrapods should mitigate interfacial charge recombination as well as bolster the stability of the film. Finally, other dyes and electrolytes can be tested for the ZnO nanotetarpods based photoanodes and could yield unexpected good results. The reason for this is simple, the dyes and electrolytes used so far are commonly optimized for $TiO_2$ but not necessarily for ZnO. In concluding this review, we strongly believe that there is a good potential for applications of branched semiconductor nanostructures in mesoscopic solar cells.

**Acknowledgements** This work was supported by the Research Grants Council of Hong Kong under the General Research Funds (No. 604809). We wish to thank all those who contributed to the work reviewed here.

## References

1. O'Regan B, Gratzel M. A low-cost, high-efficiency solar-cell based on dye-sensitized colloidal $TiO_2$ films. Nature, 1991, 353(6346): 737–740
2. Nazeeruddin M K, Kay A, Rodicio I, Humphry-baker R, Muller E, Liska P, Vlachopoulos N, Gratzel M. Conversion of light to electricity by Cis-X2bis(2,2'-bipyridyl-4,4'-dicarboxylate)ruthenium(Ii) charge-transfer sensitizers (X = $Cl^-$, $Br^-$, $I^-$, $CN^-$, and $SCN^-$) on nanocrystalline $TiO_2$ electrodes. Journal of the American Chemical Society, 1993, 115(14): 6382–6390
3. Martinson A B F, Hamann T W, Pellin M J, Hupp J T. New architectures for dye-senstized solar cells. Chemistry-A European Journal, 2008, 14(15): 4458–4467
4. Ku C H, Wu J J. Electron transport properties in ZnO nanowire array/nanoparticle composite dye-sensitized solar cells. Applied Physics Letters, 2007, 91(9): 093117
5. Feng X J, Shankar K, Varghese O K, Paulose M, Latempa T J, Grimes C A. Vertically aligned single crystal $TiO_2$ nanowire arrays grown directly on transparent conducting oxide coated glass: synthesis details and applications. Nano Letters, 2008, 8(11): 3781–3786
6. Jiang C Y, Sun X W, Tan K W, Lo G Q, Kyaw A K K, Kwong D L. High-bendability flexible dye-sensitized solar cell with a nanoparticle-modified ZnO-nanowire electrode. Applied Physics Letters, 2008, 92(14): 143101
7. Chen W, Zhang H F, Hsing I M, Yang S H. A new photoanode architecture of dye sensitized solar cell based on ZnO nanotetrapods with no need for calcination. Electrochemistry Communications, 2009, 11(5): 1057–1060
8. Yoshida T, Zhang J B, Komatsu D, Sawatani S, Minoura H, Pauporte T, Lincot D, Oekermann T, Schlettwein D, Tada H, Wohrle D, Funabiki K, Matsui M, Miura H, Yanagi H. Electrodeposition of inorganic/organic hybrid thin films. Advanced Functional Materials, 2009, 19(1): 17–43
9. Qiu Y C, Chen W, Yang S H. Facile hydrothermal preparation of hierarchically assembled, porous single-crystalline ZnO nanoplates and their application in dye-sensitized solar cells. Journal of Materials Chemistry, 2010, 20(5): 1001–1006
10. Chen W, Qiu Y C, Zhong Y C, Wong K S, Yang S H. High-Efficiency Dye-Sensitized Solar Cells Based on the Composite Photoanocles of $SnO_2$ Nanoparticles/ZnO Nanotetrapods. Journal of Physical Chemistry A, 2010, 114(9): 3127–3138
11. Chen W, Qiu Y C, Yang S H. A new ZnO nanotetrapods/$SnO_2$ nanoparticles composite photoanode for high efficiency flexible dye-sensitized solar cells. Physical Chemistry Chemical Physics, 2010, 12(32): 9494–9501
12. Qiu Y C, Chen W, Yang S H. Double-layered photoanodes from variable-size anatase $TiO_2$ nanospindles: a candidate for high-efficiency dye-sensitized solar cells. Angewandte Chemie International Edition, 2010, 49(21): 3675–3679
13. Law M, Greene L E, Johnson J C, Saykally R, Yang P D. Nanowire dye-sensitized solar cells. Nature Materials, 2005, 4(6): 455–459
14. Liu B, Aydil E S. Growth of oriented single-crystalline rutile $TiO_2$ nanorods on transparent conducting substrates for dye-sensitized solar cells. Journal of the American Chemical Society, 2009, 131 (11): 3985–3990
15. Zhu K, Neale N R, Miedaner A, Frank A J. Enhanced charge-collection efficiencies and light scattering in dye-sensitized solar cells using oriented $TiO_2$ nanotubes arrays. Nano Letters, 2007, 7 (1): 69–74
16. Yamaguchi T, Tobe N, Matsumoto D, Arakawa H. Highly efficient plastic substrate dye-sensitized solar cells using a compression method for preparation of $TiO_2$ photoelectrodes. Chemical Communications, 2007, (45): 4767–4769
17. Chen C Y, Wang M K, Li J Y, Pootrakulchote N, Alibabaei L, Ngoc-le C H, Decoppet J D, Tsai J H, Grätzel C, Wu C G, Zakeeruddin S M, Grätzel M. Highly efficient light-harvesting ruthenium sensitizer for thin-film dye-sensitized solar cells. ACS Nano, 2009, 3(10): 3103–3109
18. Dürr M, Schmid A, Obermaier M, Rosselli S, Yasuda A, Nelles G. Low-temperature fabrication of dye-sensitized solar cells by transfer of composite porous layers. Nature Materials, 2005, 4(8): 607–611
19. Murakami T N, Kijitori Y, Kawashima N, Miyasaka T. UV light-assisted chemical vapor deposition of $TiO_2$ for efficiency development at dye-sensitized mesoporous layers on plastic film electrodes. Chemistry Letters, 2003, 32(11): 1076–1077
20. Zhang D S, Yoshida T, Minoura H. Low-temperature fabrication of efficient porous titania photoelectrodes by hydrothermal crystallization at the solid/gas interface. Advanced Materials (Deerfield Beach, Fla.), 2003, 15(10): 814–817
21. Uchida S, Timiha M, Takizawa H, Kawaraya M.Flexible dye-sensitized solar cells by 28 GHz microwave irradiation. Journal of Photochemistry and Photobiology a-Chemistry, 2004, 164(1–3): 93–96

22. Zhang Q F, Dandeneau C S, Zhou X Y, Cao G Z. ZnO Nanostructures for dye-sensitized solar cells. Advanced Materials (Deerfield Beach, Fla.), 2009, 21(41): 4087–4108
23. Liu X Z, Luo Y H, Li H, Fan Y Z, Yu Z X, Lin Y, Chen L Q, Meng Q B. Room temperature fabrication of porous ZnO photoelectrodes for flexible dye-sensitized solar cells. Chemical Communications, 2007, (27): 2847–2849
24. Shi Y T, Zhan C, Wang L D, Ma B B, Gao R, Zhu Y F, Qiu Y. Polydisperse spindle-shaped ZnO particles with their packing micropores in the photoanode for highly efficient quasi-solid dye-sensitized solar cells. Advanced Functional Materials, 2010, 20(3): 437–444
25. Zhang Q F, Dandeneau C S, Zhou X Y, Cao G Z. ZnO Nanostructures for dye-sensitized solar cells. Advanced Materials (Deerfield Beach, Fla.), 2009, 21(41): 4087–4108
26. Hsu Y F, Xi Y Y, Yip C T, Djurisic A B, Chan W K. Dye-sensitized solar cells using ZnO tetrapods. Journal of Applied Physics, 2008, 103(8): 083114
27. Qiu Y F, Yang S H. ZnO nanotetrapods: Controlled vapor-phase synthesis and application for humidity sensing. Advanced Functional Materials, 2007, 17(8): 1345–1352
28. Chiu W H, Lee C H, Cheng H M, Lin H F, Liao S C, Wu J M, Hsieh W F. Efficient electron transport in tetrapod-like ZnO metal-free dye-sensitized solar cells. Energy & Environmental Science, 2009, 2 (6): 694–698
29. Bacsa R R, Dexpert-Ghys J, Verelst M, Falqui A, Machado B, Bacsa W S, Chen P, Zakeeruddin S M, Graetzel M, Serp P. Synthesis and structure-property correlation in shape-controlled ZnO nanoparticles prepared by chemical vapor synthesis and their application in dye-sensitized solar cells. Advanced Functional Materials, 2009, 19(6): 875–886
30. Horiuchi H, Katoh R, Hara K, Yanagida M, Murata S, Arakawa H, Tachiya M. Electron injection efficiency from excited N3 into nanocrystalline ZnO films: Effect of (N3-$Zn^{2+}$) aggregate formation. Journal of Physical Chemistry B, 2003, 107(11): 2570–2574
31. Keis K, Lindgren J, Lindquist S E, Hagfeldt A. Studies of the adsorption process of Ru complexes in nanoporous ZnO electrodes. Langmuir, 2000, 16(10): 4688–4694
32. Chou T P, Zhang Q F, Fryxell G E, Cao G Z. Hierarchically structured ZnO film for dye-sensitized solar cells with enhanced energy conversion efficiency. Advanced Materials (Deerfield Beach, Fla.), 2007, 19(18): 2588–2592
33. Wang Q, Ito S, Grätzel M, Fabregat-Santiago F, Mora-Seró I, Bisquert J, Bessho T, Imai H. Characteristics of high efficiency dye-sensitized solar cells. Journal of Physical Chemistry B, 2006, 110 (50): 25210–25221
34. Wang Q, Moser J E, Grätzel M. Electrochemical impedance spectroscopic analysis of dye-sensitized solar cells. Journal of Physical Chemistry B, 2005, 109(31): 14945–14953
35. Fabregat-Santiago F, Bisquert J, Garcia-Belmonte G, Boschloo G, Hagfeldt A. Influence of electrolyte in transport and recombination in dye-sensitized solar cells studied by impedance spectroscopy. Solar Energy Materials and Solar Cells, 2005, 87(1–4): 117–131
36. Fabregat-Santiago F, Barea E M, Bisquert J, Mor G K, Shankar K, Grimes C A. High carrier density and capacitance in $TiO_2$ nanotube arrays induced by electrochemical doping. Journal of the American Chemical Society, 2008, 130(34): 11312–11316
37. Wang Q, Zhang Z, Zakeeruddin S M, Gratzel M. Enhancement of the performance of dye-sensitized solar cell by formation of shallow transport levels under visible light illumination. Journal of Physical Chemistry C, 2008, 112(17): 7084–7092
38. Tan B, Wu Y Y. Dye-sensitized solar cells based on anatase $TiO_2$ nanoparticle/nanowire composites. Journal of Physical Chemistry B, 2006, 110(32): 15932–15938
39. Thavasi V, Renugopalakrishnan V, Jose R, Ramakrishna S. Controlled electron injection and transport at materials interfaces in dye sensitized solar cells. Materials Science and Engineering R Reports, 2009, 63(3): 81–99
40. Gan X Y, Li X M, Gao X D, Zhuge F W, Yu W D. ZnO nanowire/$TiO_2$ nanoparticle photoanodes prepared by the ultrasonic irradiation assisted dip-coating method. Thin Solid Films, 2010, 518(17): 4809–4812
41. Yodyingyong S, Zhang Q F, Park K, Dandeneau C S, Zhou X Y, Triampo D, Cao G Z. ZnO nanoparticles and nanowire array hybrid photoanodes for dye-sensitized solar cells. Applied Physics Letters, 2010, 96(7): 073115
42. Kumara G R R A, Tennakone K, Kottegoda I R M, Bandaranayake P K M, Konno A, Okuya M, Kaneko S, Murakami K. Efficient dye-sensitize photoelectrochemical cells made from nanocrystalline tin(IV) oxide-zinc oxide composite films. Semiconductor Science and Technology, 2003, 18(4): 312–318
43. Niinobe D, Makari Y, Kitamura T, Wada Y, Yanagida S. Origin of enhancement in open-circuit voltage by adding ZnO to nanocrystalline $SnO_2$ in dye-sensitized solar cells. Journal of Physical Chemistry B, 2005, 109(38): 17892–17900
44. Nozik A J, Memming R. Physical chemistry of semiconductor-liquid interfaces. Journal of Physical Chemistry, 1996, 100(31): 13061–13078
45. Tan B, Toman E, Li Y G, Wu Y Y. Zinc stannate ($Zn_2SnO_4$) dye-sensitized solar cells. Journal of the American Chemical Society, 2007, 129(14): 4162–4163
46. Hore S, Nitz P, Vetter C, Prahl C, Niggemann M, Kern R. Scattering spherical voids in nanocrystalline $TiO_2$- enhancement of efficiency in dye-sensitized solar cells. Chemical Communications, 2005, (15): 2011–2013
47. Ferber J, Luther J. Computer simulations of light scattering and absorption in dye-sensitized solar cells. Solar Energy Materials and Solar Cells, 1998, 54(1–4): 265–275
48. Kay A, Gratzel M. Dye-sensitized core-shell nanocrystals: Improved efficiency of mesoporous tin oxide electrodes coated with a thin layer of an insulating oxide. Chemistry of Materials, 2002, 14(7): 2930–2935
49. Ito S, Murakami T N, Comte P, Liska P, Gratzel C, Nazeeruddin M K, Gratzel M. Fabrication of thin film dye sensitized solar cells with solar to electric power conversion efficiency over 10%. Thin Solid Films, 2008, 516(14): 4613–4619
50. Jing B W, Zhang H, Zhang M H, Lu Z H, Shen T. Ruthenium(II) thiocyanate complexes containing 4 '-(4-phosphonatophenyl)-2,2 ': 6 ',2 “-terpyridine: synthesis, photophysics and photosensitization to nanocrystalline $TiO_2$ electrodes. Journal of Materials Chemistry, 1998, 8(9): 2055–2060
51. Tennakone K, Kumara G R R A, Kottegoda I R M, Perera V P S. An

efficient dye-sensitized photoelectrochemical solar cell made from oxides of tin and zinc. Chemical Communications, 1999, (1): 15–16

52. Fukai Y, Kondo Y, Mori S, Suzuki E. Highly efficient dye-sensitized $SnO_2$ solar cells having sufficient electron diffusion length. Electrochemistry Communications, 2007, 9(7): 1439–1443
53. Koide N, Islam A, Chiba Y, Han L Y. Improvement of efficiency of dye-sensitized solar cells based on analysis of equivalent circuit. Journal of Photochemistry and Photobiology a-Chemistry, 2006, 182(3): 296–305
54. Wang Z S, Kawauchi H, Kashima T, Arakawa H. Significant influence of $TiO_2$ photoelectrode morphology on the energy conversion efficiency of N719 dye-sensitized solar cell. Coordination Chemistry Reviews, 2004, 248(13–14): 1381–1389
55. Grätzel M. Mesoscopic solar cells for electricity and hydrogen production from sunlight. Chemistry Letters, 2005, 34(1): 8–13
56. Koops S E, Durrant J R. Transient emission studies of electron injection in dye sensitised solar cells. Inorganica Chimica Acta, 2008, 361(3): 663–670
57. Koops S E, O'Regan B C, Barnes P R F, Durrant J R. Parameters influencing the efficiency of electron injection in dye-sensitized solar cells. Journal of the American Chemical Society, 2009, 131 (13): 4808–4818
58. Oekermann T, Zhang D, Yoshida T, Minoura H. Electron transport and back reaction in nanocrystalline $TiO_2$ films prepared by hydrothermal crystallization. Journal of Physical Chemistry B, 2004, 108(7): 2227–2235
59. Zhu K, Vinzant T B, Neale N R, Frank A J. Removing structural disorder from oriented $TiO_2$ nanotube arrays: reducing the dimensionality of transport and recombination in dye-sensitized solar cells. Nano Letters, 2007, 7(12): 3739–3746
60. Demir M M, Munoz-Espi R, Lieberwirth I, Wegner G. Precipitation of monodisperse ZnO nanocrystals via acid-catalyzed esterification of zinc acetate. Journal of Materials Chemistry, 2006, 16(28): 2940–2947
61. van de Lagemaat J, Frank A J. Nonthermalized electron transport in dye-sensitized nanocrystalline $TiO_2$ films: Transient photocurrent and random-walk modeling studies. Journal of Physical Chemistry B, 2001, 105(45): 11194–11205
62. Colodrero S, Mihi A, Haggman L, Ocana M, Boschloo G, Hagfeldt A, Miguez H. Porous one-dimensional photonic crystals improve the power-conversion efficiency of dye-sensitized solar cells. Advanced Materials (Deerfield Beach, Fla.), 2009, 21(7): 764–770
63. Park N G, Kim K M, Kang M G, Ryu K S, Chang S H, Shin Y J. Chemical sintering of nanoparticles: A methodology for low-temperature fabrication of dye-sensitized $TiO_2$ films. Advanced Materials (Deerfield Beach, Fla.), 2005, 17(19): 2349–2353
64. Zhang D S, Yoshida T, Oekermann T, Furuta K, Minoura H. Room-temperature synthesis of porous nanoparticulate $TiO_2$ films for flexible dye-sensitized solar cells. Advanced Functional Materials, 2006, 16(9): 1228–1234
65. Toivola M, Halme J, Miettunen K, Aitola K, Lund P D. Nanostructured dye solar cells on flexible substrates-review. International Journal of Energy Research, 2009, 33(13): 1145–1160
66. Zhang Q F, Chou T P, Russo B, Jenekhe S A, Cao G Z. Aggregation of ZnO nanocrystallites for high conversion efficiency in dye-sensitized solar cells. Angewandte Chemie International Edition, 2008, 47(13): 2402–2406
67. Han L Y, Koide N, Chiba Y, Mitate T. Modeling of an equivalent circuit for dye-sensitized solar cells. Applied Physics Letters, 2004, 84(13): 2433–2435
68. Han L Y, Koide N, Chiba Y, Islam A, Mitate T. Modeling of an equivalent circuit for dye-sensitized solar cells: improvement of efficiency of dye-sensitized solar cells by reducing internal resistance. Comptes Rendus. Chimie, 2006, 9(5–6): 645–651
69. Chen H W, Hsu C Y, Chen J G, Lee K M, Wang C C, Huang K C, Ho K C. Plastic dye-sensitized photo-supercapacitor using electrophoretic deposition and compression methods. Journal of Power Sources, 2010, 195(18): 6225–6231
70. Grinis L, Kotlyar S, Ruhle S, Grinblat J, Zaban A. Conformal nano-sized inorganic coatings on mesoporous $TiO_2$ films for low-temperature dye-sensitized solar cell fabrication. Advanced Functional Materials, 2010, 20(2): 282–288